Three-Dimensional UAV-to-UAV Channels: Modeling, Simulation, and Capacity Analysis

Linzhou Zeng, *Member, IEEE*, Xuewen Liao, *Member, IEEE*, Zhangfeng Ma, *Member, IEEE*, Baiping Xiong, *Graduate Student Member, IEEE*, Hao Jiang, *Member, IEEE*, and Zhen Chen, *Senior Member, IEEE*

***Abstract*—A 3-D arbitrary-elevation two-cylinder reference model is proposed for multiple-input–multiple-output (MIMO) air-to-air communications in unmanned aerial vehicle (UAV) channels. This model accounts for not only the Line-of-Sight (LoS) but also the single-bounced at the transmitter (SBT) and the single-bounced at the receiver (SBR), as well as the double-bounced (DB) rays. Therefore, it is endowed with a high adaptability to various UAV-to-UAV communication scenarios. From the reference model, a closed-form expression of the space-time correlation function (ST-CF) is derived. This expression is shown to be the generalizations of many existing correlation functions from the 2-D one-ring, the 3-D low-elevation one-cylinder, the 2-D two-ring, and the 3-D low-elevation two-cylinder model. Corresponding deterministic and stochastic simulation models are also developed in addition to the reference model. The well agreements between the channel capacities obtained from the simulation models and those from the derived ST-CF not only display the usefulness of the simulators but also confirm the correctness of the derivations. Based on the derived closed-form ST-CF, the effects of some model parameters on the capacity are evaluated in a computationally efficient manner.**

***Index Terms*—Channel capacity, channel correlation, geometry-based stochastic model (GBSM), unmanned aerial vehicle (UAV)-to-UAV communications.**

Manuscript received 6 August 2023; revised 22 September 2023; accepted 11 October 2023. Date of publication 19 October 2023; date of current version 7 March 2024. This work was supported in part by the Natural Science Foundation of Hunan Province under Grant 2023JJ40607 and Grant 2023JJ50266; in part by the Beijing Engineering Research Center of High-Speed Railway Broadband Mobile Communications under Grant BHRC-2022-3; and in part by the National Natural Science Foundation of China under Grant 62101275. *(Corresponding author: Linzhou Zeng.)*

Linzhou Zeng is with the School of Information Science and Engineering, Hunan Institute of Science and Technology, Yueyang 414006, China; and also with the School of Information and Communications Engineering, Faculty of Electronic and Information Engineering, Xi'an Jiaotong University, Xi'an 710049, China (e-mail: linzhou.zeng@hnist.edu.cn).

Xuewen Liao is with the School of Information and Communications Engineering, Faculty of Electronic and Information Engineering, Xi'an Jiaotong University, Xi'an 710049, China (e-mail: yeplos@mail.xjtu.edu.cn).

Zhangfeng Ma is with the School of Information Science and Engineering, Shaoyang University, Shaoyang 422000, China (e-mail: zhangfeng.ma@vip.126.com).

Baiping Xiong is with the National Mobile Communications Research Laboratory, Southeast University, Nanjing 210096, China (e-mail: xiongbp@seu.edu.cn).

Hao Jiang is with the School of Artificial Intelligence/School of Future Technology, Nanjing University of Information Science and Technology, Nanjing 210044, China, and also with the National Mobile Communications Research Laboratory, Southeast University, Nanjing 210096, China (e-mail: jianghao@nuist.edu.cn).

Zhen Chen is with the School of Electronic and Information Engineering, South China University of Technology, Guangzhou 510641, China (e-mail: chenz@scut.edu.cn).

Digital Object Identifier 10.1109/JIOT.2023.3325945

I. Introduction

THE PAST few years have witnessed a growing interest in communications assisted by unmanned aerial vehicles (UAVs) as they become affordable and flexible [1], [2]. As a supplement to traditional terrestrial cellular networks [3], UAV-assisted communications can provide dynamic deployment capabilities and connectivity coverage extensions [4]. To establish a high-speed and large-coverage UAV network, two different kinds of communication scenarios need to be considered, i.e., UAV-to-ground (U2G) and UAV-to-UAV (U2U) [5], [6]. In the U2G communications, the UAV can serve as an aerial mobile base that provides a highly flexible connection to the ground station (GS) [7], [8]. The U2U communications, on the other hand, can be used to build a UAV-enabled multihop link for data transmission, allowing data sharing among the elements of a UAV virtual antenna array [9]. With these promising applications, it is necessary to quantitatively study the benefits brought by the UAVs under different propagation environments [10]. To this end, a prerequisite task for us is to develop practical yet easy-to-use U2U channel models that capture some unique UAV-related behaviors, e.g., the UAV's locations, positions, and motions [11].

Recently, some efforts have been made to characterize the U2U channels. Existing U2U channel modeling approaches can be broadly categorized into the deterministic ones and the statistical ones. The most common deterministic modeling approach is based on measurements [12], [13], [14], [15]. In [12], the Rice channel model was extended to UAV air-to-air (A2A) communication environments by introducing the effects of the UAV's altitude based on some measurement results. In [13], another preliminary measured result was reported to characterize the low-altitude UAV A2A channels, where both the large-scale fading and the small-scale fading were considered. Ede et al. [14] conducted a measurement campaign to study the large scale fading of A2A wireless UAV channels. In addition, the ray-tracing method, as another widely used deterministic modeling approach, was combined with the measured-based one in [15] for A2A channel characterization, where a tapped-delay-line model was also developed. These deterministic channel models in general have high fidelity to the measured environments, but unfortunately have relatively low generality as they are environment-specific.

In contrast to the deterministic models above, the statistical ones have better universality because they are not confined to a certain environment but are instead adaptive to various scenarios through parameter adjustments. Specifically, as for UAV A2A channel modeling, the two-ray model is a commonly seen one [16], [17], which accounts for the Line-of-Sight (LoS) component and the ground reflection components. This kind of model is simple and convenient, yet it barely give consideration to the diffuse components induced by ambient scatterers, such as buildings, trees, or vehicles. As a result, the two-ray model is not suitable to characterize the low-altitude UAV A2A channels, especially in urban areas. To fully consider the scattered components, some researchers have applied the geometry-based stochastic modeling approach to the U2U channels [18], [19], [20], [21], [22], [23], [24], [25]. In [18] and [19], a single-cylinder geometry-based stochastic model (GBSM) was proposed for wideband nonstationary UAV A2A channels, where the UAV's three-dimensional (3-D) random trajectories were included. Based on this model, the impact of the UAV's jitter was further investigated in [20]. Moreover, this single-cylinder geometrical model was extended in [21] and [22] to millimeter-wave UAV-based communications by introducing a two-state continuous-time Markov model that describes the dynamic appearance/disappearance properties of the scatterers. Apart from the cylinder-based models, some other regular-shaped GBSMs have also been used to characterize the UAV A2A channels. For example, two ellipsoid-based models were proposed in [23] and [24] and a sphere-based one was reported in [25]. Based on the GBSMs proposed in these works, some essential channel characteristics, including the space-time correlation function (ST-CF) and the Doppler power spectrum density (PSD), were derived, and the impacts of some unique UAV-related parameters on the channel characteristics were then analyzed, which led to useful guidance for the design of U2U communication systems.

Ever since the one-ring model by Jakes, geometrical models have been well researched for channel characterization and capacity analysis. This one-ring model was extended in [26] to derive the spatial fading correlation and analyze the capacity for fixed-to-fixed multiple-input–multiple-output (MIMO) channels, and it was further generalized in [27] to obtain the ST-CF and quantify the effects of the propagation channel characteristics on the capacity for fixed-to-mobile MIMO channels. To consider the scattering at both ends of the radio link rather than only one side, a two-ring model was proposed in [28] to study the effects of ST-CF on the fixed-to-mobile MIMO channels. Both the one-ring model and the two-ring model are 2-D and thus only valid for certain environments where the propagating waves travel in the horizontal plane. In order to account for the waves that propagate not completely horizontally (e.g., due to dispersion or diffraction from buildings down to streets), Zajić and Stüber proposed a low-elevation two-cylinder model in [29], which allowed them to derive a closed-form ST-CF and to evaluate the effect of the ST-CF on the mobile-to-mobile channel capacity for 3-D nonisotropic scattering environments. Nevertheless, this two-cylinder still assumed 2-D moving low-elevated stations, which is suitable for terrestrial vehicle-to-vehicle (V2V) communications but unfortunately not so appropriate for U2G communications where the UAV can be in 3-D motion at a considerable altitude. Given this problem, reported in [30] was an arbitrary-elevation one-cylinder model that took into account the vertical component of the UAV's velocity, and this model was modified into a polarized one in [31] to investigate the impact of some key factors, such as the cross-polarization and antenna spacing on the UAV channel capacity.

While there are a number of geometrical models that can be used to evaluate the capacity of the V2V channels or the U2G channels, still widely missing in literature is a GBSM that enables us to properly abstract the U2U propagation environments and, thereby, allows us to efficiently analyze the corresponding channel capacity. Different from the V2V communications that are terrestrial [32], [33], the U2U communications are aerial and thus fully 3-D in terms of both the environmental scattering and the terminal movements, which means that the V2V channel models cannot be directly used for U2U channels. Meanwhile, compared to the U2G communications where the aerial station is often much higher than the GS as well as the ground scatterers [34], [35], the U2U communications often have the transmitter (Tx) and receiver (Rx) in co-equal status at similar altitudes. Hence, there is no reason for us to neglect the scattering at each side of them, which implies that the widely used arbitrary-elevation one-cylinder model is not quite applicable to the characterization of U2U wireless channels. But it should also be pointed out that the similarity between the U2U channels and the V2V or U2G ones is also obvious: they are all mobile radio channels with multiple antennas equipped on the ends. This gives us the faith that it is viable to adopt the geometry-based stochastic modeling approach to the modeling and capacity analysis of U2U channels. Motivated by that, in this article, we propose a generic geometrical model for the U2U MIMO channels that accounts for the 3-D locations and movements of the UAVs as well as the 3-D scattering at both sides, where the received signal is a superposition of the LoS, the single-bounced at the Tx (SBT), the single-bounced at the Rx (SBR), and the double-bounced (DB) rays. The novelties and contributions of this article are as follows.

1) An arbitrary-elevation two-cylinder GBSM is proposed to characterize the U2U Rician fading channels, which captures the arbitrary altitude and vertical movement of the UAV. It is an extension of the low-elevation two-cylinder GBSM that only applies to terrestrial scenarios where the two ground stations move at similarly low altitudes. By adjusting the parameters, the proposed model is adaptable to a variety of U2U communication scenarios (low/high-altitude, dense/sparse-scattering, or urban/rural-area).
2) A closed-form expression of the ST-CF is derived from the proposed arbitrary-elevation two-cylinder model using a spatial-vector-based method, which, compared to the conventional geometric-relation-based method, exhibits stronger ability to extract the geometric information.
3) The derived theoretical statistics are shown to embody many of the ones previously reported from the 2-D

or 3-D geometrical models as special cases. What is more, the channel capacities obtained from the theoretical correlations agree well with those in the simulated results, demonstrating the correctness of the derivations.

4) The impacts of some model parameters on the channel capacities are studied at a low computational cost using the closed-form correlation function. Some interesting observations are given, which are helpful for the design of U2U MIMO communication systems.

The remainder of this article is as follows. Section II describes the reference channel model and derives its statistical properties. Section III presents the corresponding simulation models. Finally, conclusions are drawn in Section V.

Notation: The lightfaced roman letters (e.g., x or X), the boldfaced roman ones (e.g., $\boldsymbol{x}$ and $\boldsymbol{X}$), and the boldfaced italic uppercase ones (e.g., $\mathbf{X}$) stand for the scalars, the vectors, and the matrices, respectively. Those boldfaced roman but with a hat overhead (e.g., $\hat{\boldsymbol{x}}$) represent the corresponding unit vectors. For scalars, mod is the modulo operator, $(\cdot)^*$ is the complex conjugate operator, $\mathbb{E}[\,\cdot\,]$ is the expectation operator, $\mathcal{F}\{\cdot\}$ is the Fourier transform operator, and $*$ is the convolution operator. For vectors, $|\cdot|$ denotes the vector norm operation, $\langle\cdot,\cdot\rangle$ denotes the vectors angle operation, $(\cdot)^{\mathrm{T}}$ denotes the vector transpose operation, $\cdot$ denotes the dot product operation, and $\times$ denotes the cross product operation. For matrices, $(\cdot)^{1/2}$ symbolizes the matrix square root, $(\cdot)^{\mathrm{T}}$ symbolizes the matrix transpose, $\mathrm{vec}(\cdot)$ symbolizes the matrix vectorization, $(\cdot)^{\dagger}$ symbolizes the matrix conjugate transpose, and $\det(\cdot)$ symbolizes the matrix determinant.

II. Reference Model for U2U MIMO Channels

Let us consider a narrowband U2U MIMO communication system with M_T transmit and M_R receive omnidirectional antenna elements, which are configured as two uniform linear arrays (ULAs) centered at the points O_T and O_R, respectively. The pth transmit antenna is denoted by $A_T^{(p)}$ and the qth receive antenna is denoted by $A_R^{(q)}$, where $1 \le p \le M_T$ and $1 \le q \le M_R$. The Tx and Rx move with velocities $\boldsymbol{v}_T$ and $\boldsymbol{v}_R$, respectively, and the moving direction of the Tx (Rx) are characterized by the angle pair γ_T (γ_R) and ξ_T (ξ_R). As in Fig. 1, we assume that N_1 transmit scatterers are distributed on the surface of one cylinder of radius R_1 at the Tx side, and that N_2 receive ones are distributed on the surface of the other cylinder of radius R_2 at the Rx side. The n_1th transmit scatterer is denoted by $S_T^{(n_1)}$ and the n_2th receive scatterer is denoted by $S_R^{(n_2)}$, where $1 \le n_1 \le N_1$ and $1 \le n_2 \le N_2$, respectively. For $S_T^{(n_1)}$, we use $\alpha_T^{(n_1)}$ and $\beta_T^{(n_1)}$ to denote its azimuth and elevation angle relative to O_T, also known as the azimuth and the elevation Angle of Departure (AoD), respectively; for $S_R^{(n_2)}$, we use $\alpha_R^{(n_2)}$ and $\beta_R^{(n_2)}$ to denote its azimuth and the elevation angle relative to O_R, also known as the azimuth and the elevation Angle of Arrival (AoA), respectively. Besides, the displacement vectors from $A_T^{(p)}$ to $S_T^{(n_1)}$, from $S_T^{(n_1)}$ to $S_R^{(n_2)}$, and from $S_R^{(n_2)}$ to $A_R^{(q)}$, are represented by $\boldsymbol{d}_{pn_1}$, $\boldsymbol{d}_{n_1n_2}$, and $\boldsymbol{d}_{n_2q}$, respectively. Other symbols are explained in Table I.

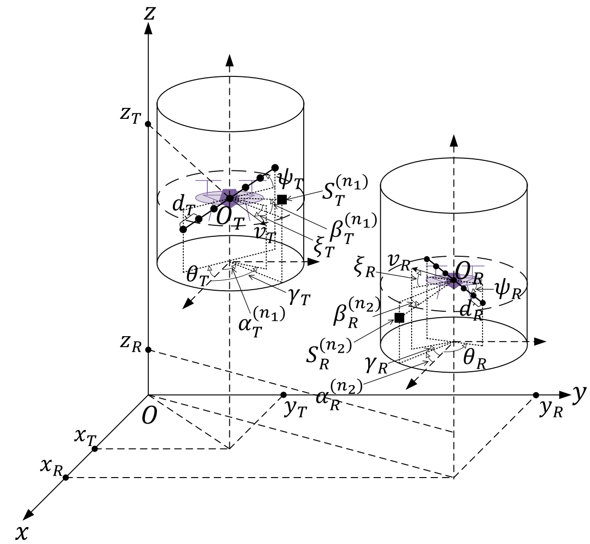

Fig. 1. Proposed 3-D two-cylinder GBSM with small drones as example. Each cylinder is an abstraction of the local scatterers around the respective UAV station. In reality, those scattering objects may include buildings and streetlights for low-altitude small-size U2U communications, or may be the wings on the aircraft itself for high-altitude large-size U2U communications.

TABLE I
Denotations of Symbols in the Model

Symbol	Denotation
O	The origin of the Cartesian coordinate system.
O_T, O_R	The center of the ULA at the Tx and at the Rx, respectively.
R_1, R_2	The radius of the cylinder at the Tx side and at the Rx side, respectively.
$A_T^{(p)}$, $A_R^{(q)}$	The pth antenna at the Tx and the qth antenna at the Rx, respectively.
$S_T^{(n_1)}$, $S_R^{(n_2)}$	The n_1th effective scatterer at the Tx side and the n_2th effective scatterer at the Rx side, respectively.
d_T, d_R	The spacing between any two adjacent antenna elements at the Tx and at the Rx, respectively.
θ_T, θ_R	The azimuth angle (relative to the $+x$-axis) of the ULA at the Tx and at the Rx, respectively.
ψ_T, ψ_R	TThe elevation angle (relative to the xy-palne) of the ULA at the Tx and at the Rx, respectively.
$\boldsymbol{v}_T$, $\boldsymbol{v}_R$	The velocity vector of the Tx and of the Rx, respectively.
γ_T, γ_R	The azimuth angle (relative to the $+x$-axis) of $\boldsymbol{v}_T$ and of $\boldsymbol{v}_R$, respectively.
ξ_T, ξ_R	The elevation angle (relative to the xy-plane) of $\boldsymbol{v}_T$ and of $\boldsymbol{v}_R$, respectively.
$\boldsymbol{d}_{pq}$, $\boldsymbol{d}_{TR}$	The displacement vector from $A_T^{(p)}$ to $A_R^{(q)}$ and from O_T to O_R, respectively.
$\boldsymbol{d}_{pn_1}$, $\boldsymbol{d}_{Tn_1}$	The displacement vector from $A_T^{(p)}$ to $S_T^{(n_1)}$ and from O_T to $S_T^{(n_1)}$, respectively.
$\boldsymbol{d}_{n_2q}$, $\boldsymbol{d}_{n_2R}$	The displacement vector from $S_R^{(n_2)}$ to $A_R^{(q)}$ and from $S_R^{(n_2)}$ to O_R, respectively.
$\boldsymbol{d}_{Tp}$, $\boldsymbol{d}_{Rq}$	The displacement vector from O_T to $A_T^{(p)}$ and from O_R to $A_R^{(q)}$, respectively.

The complex channel gain between $A_T^{(p)}$ and $A_R^{(q)}$ is a sum of the LoS, SBT, SBR, and DB components, i.e.,

$$h_{pq}(t) = \sqrt{\frac{K}{K+1}}h_{pq}^{\mathrm{LoS}}(t) + \sqrt{\frac{\eta_{\mathrm{SBT}}}{K+1}}h_{pq}^{\mathrm{SBT}}(t) + \sqrt{\frac{\eta_{\mathrm{SBR}}}{K+1}}h_{pq}^{\mathrm{SBR}}(t) + \sqrt{\frac{\eta_{\mathrm{DB}}}{K+1}}h_{pq}^{\mathrm{DB}}(t) \quad (1)$$

where K is the Rician factor, and the nonnegative parameters η_{SBT}, η_{SBR}, and η_{DB} specify the contributions of the SBT, the SBR, and the DB components, respectively, to the total scattered power, which satisfy $\eta_{\mathrm{SBT}}+\eta_{\mathrm{SBR}}+\eta_{\mathrm{DB}}=1$. Based on the model, we have

$$h_{pq}^{\mathrm{LoS}}(t)=e^{-j\frac{2\pi}{\lambda}|\boldsymbol{d}_{pq}|}e^{j2\pi(f_{T\max}\cos\langle\boldsymbol{v}_T,\boldsymbol{d}_{pq}\rangle-f_{R\max}\cos\langle\boldsymbol{v}_R,\boldsymbol{d}_{pq}\rangle)t} \quad (2)$$

$$h_{pq}^{\mathrm{SBT}}(t)=\lim_{N_1\to\infty}\frac{1}{\sqrt{N_1}}\sum_{n_1=1}^{N_1}e^{j\phi_{n_1}}e^{-j\frac{2\pi}{\lambda}(|\boldsymbol{d}_{pn_1}|+|\boldsymbol{d}_{n_1q}|)} e^{j2\pi(f_{T\max}\cos\langle\boldsymbol{v}_T,\boldsymbol{d}_{pn_1}\rangle-f_{R\max}\cos\langle\boldsymbol{v}_R,\boldsymbol{d}_{n_1q}\rangle)t} \quad (3)$$

$$h_{pq}^{\mathrm{SBR}}(t)=\lim_{N_2\to\infty}\frac{1}{\sqrt{N_2}}\sum_{n_2=1}^{N_2}e^{j\phi_{n_2}}e^{-j\frac{2\pi}{\lambda}(|\boldsymbol{d}_{pn_2}|+|\boldsymbol{d}_{n_2q}|)} e^{j2\pi(f_{T\max}\cos\langle\boldsymbol{v}_T,\boldsymbol{d}_{pn_2}\rangle-f_{R\max}\cos\langle\boldsymbol{v}_R,\boldsymbol{d}_{n_2q}\rangle)t} \quad (4)$$

$$h_{pq}^{\mathrm{DB}}(t)=\lim_{N_1,N_2\to\infty}\frac{1}{\sqrt{N_1N_2}}\sum_{n_1=1}^{N_1}\sum_{n_2=1}^{N_2}e^{j\phi_{n_1n_2}} e^{-j\frac{2\pi}{\lambda}(|\boldsymbol{d}_{pn_1}|+|\boldsymbol{d}_{n_1n_2}|+|\boldsymbol{d}_{n_2q}|)} e^{j2\pi(f_{T\max}\cos\langle\boldsymbol{v}_T,\boldsymbol{d}_{pn_1}\rangle-f_{R\max}\cos\langle\boldsymbol{v}_R,\boldsymbol{d}_{n_2q}\rangle)t} \quad (5)$$

where λ is the carrier wavelength, $f_{T\max}=|\boldsymbol{v}_T|/\lambda$ and $f_{R\max}=|\boldsymbol{v}_R|/\lambda$ are, respectively, the maximum Doppler frequencies associated with the Tx and Rx, ϕ_{n_1} and ϕ_{n_2} are the random phase shifts induced by the n_1th transmit scatterer $S_T^{(n_1)}$ and the n_2th receive scatterer $S_R^{(n_2)}$, respectively, which are assumed to be independently uniformly distributed over the interval $[0,2\pi)$, and finally, $\phi_{n_1n_2}=(\phi_{n_1}+\phi_{n_1}) \bmod 2\pi$ is the joint phase shift caused by $S_T^{(n_1)}$ and the subsequent $S_R^{(n_2)}$, which is also uniformly distributed over $[0,2\pi)$. Unlike the significant difference between the single-bounced rays (whose AoDs are dependent on AoAs) and the DB ones (whose are independent), the triple-bounced or higher order-bounced rays are very similar to the DB ones [36]. Hence, it is unnecessary to consider them separately.

To aid further derivations, we do some useful approximations on the distances and angles that have appeared in (2)–(5). In (2), $|\boldsymbol{d}_{pq}|$ can be written as $|\boldsymbol{d}_{pq}|=\sqrt{|\boldsymbol{d}_{pT}+\boldsymbol{d}_{TR}+\boldsymbol{d}_{Rq}|^2}\approx\sqrt{|\boldsymbol{d}_{TR}|^2+2\boldsymbol{d}_{TR}\cdot(\boldsymbol{d}_{pT}+\boldsymbol{d}_{Rq})}$, where we have omitted the extremely small terms $|\boldsymbol{d}_{pT}|^2$, $|\boldsymbol{d}_{Rq}|^2$, and $2\boldsymbol{d}_{pT}\cdot\boldsymbol{d}_{Rq}$. Furthermore, using the approximation $\sqrt{1+x}\approx 1+x/2$ for $x\ll 1$, it is not difficult to obtain that $|\boldsymbol{d}_{pq}|\approx|\boldsymbol{d}_{TR}|(1+(\boldsymbol{d}_{TR}/|\boldsymbol{d}_{TR}|^2)\cdot(\boldsymbol{d}_{pT}+\boldsymbol{d}_{Rq}))=|\boldsymbol{d}_{TR}|+\hat{\boldsymbol{d}}_{TR}\cdot(-\boldsymbol{d}_{Tp}+\boldsymbol{d}_{Rq})$, where we have introduced the unit vector $\hat{\boldsymbol{d}}_{TR}=\boldsymbol{d}_{TR}/|\boldsymbol{d}_{TR}|$. Meanwhile, since $d_T, d_R\ll|\boldsymbol{d}_{TR}|$, we have $\langle\boldsymbol{v}_T,\boldsymbol{d}_{pq}\rangle\approx\langle\boldsymbol{v}_T,\boldsymbol{d}_{TR}\rangle$ and $\langle\boldsymbol{v}_R,\boldsymbol{d}_{pq}\rangle\approx\langle\boldsymbol{v}_R,\boldsymbol{d}_{TR}\rangle$; in (3), we can approximate $|\boldsymbol{d}_{pn_1}|$ and $|\boldsymbol{d}_{n_1q}|$ by $|\boldsymbol{d}_{pn_1}|\approx|\boldsymbol{d}_{Tn_1}|-\hat{\boldsymbol{d}}_{Tn_1}\cdot\boldsymbol{d}_{Tp}$ and $|\boldsymbol{d}_{n_1q}|\approx|\boldsymbol{d}_{n_1R}|+\hat{\boldsymbol{d}}_{n_1R}\cdot\boldsymbol{d}_{Rq}$, respectively, where $\hat{\boldsymbol{d}}_{Tn_1}=\boldsymbol{d}_{Tn_1}/|\boldsymbol{d}_{Tn_1}|$ and $\hat{\boldsymbol{d}}_{n_1R}=\boldsymbol{d}_{n_1R}/|\boldsymbol{d}_{n_1R}|$. At the same time, as $d_T, d_R\ll R\ll|\boldsymbol{d}_{TR}|$, we have $\langle\boldsymbol{v}_T,\boldsymbol{d}_{pn_1}\rangle\approx\langle\boldsymbol{v}_T,\boldsymbol{d}_{Tn_1}\rangle$ and $\langle\boldsymbol{v}_R,\boldsymbol{d}_{n_1q}\rangle\approx\langle\boldsymbol{v}_R,\boldsymbol{d}_{n_1R}\rangle$; in (4), $|\boldsymbol{d}_{pn_2}|$ and $|\boldsymbol{d}_{n_2q}|$ can be approximated into $|\boldsymbol{d}_{pn_2}|\approx|\boldsymbol{d}_{Tn_2}|-\hat{\boldsymbol{d}}_{Tn_2}\cdot\boldsymbol{d}_{Tp}$, and $|\boldsymbol{d}_{n_2q}|\approx|\boldsymbol{d}_{n_2R}|+\hat{\boldsymbol{d}}_{n_2R}\cdot\boldsymbol{d}_{Rq}$, respectively, where $\hat{\boldsymbol{d}}_{Tn_2}=\boldsymbol{d}_{Tn_2}/|\boldsymbol{d}_{Tn_2}|$ and $\hat{\boldsymbol{d}}_{n_2R}=\boldsymbol{d}_{n_2R}/|\boldsymbol{d}_{n_2R}|$. In the mean time, we can obtain that $\langle\boldsymbol{v}_T,\boldsymbol{d}_{pn_2}\rangle\approx\langle\boldsymbol{v}_T,\boldsymbol{d}_{Tn_2}\rangle$ and $\langle\boldsymbol{v}_R,\boldsymbol{d}_{n_2q}\rangle\approx\langle\boldsymbol{v}_R,\boldsymbol{d}_{n_2R}\rangle$; and in (5), as was just mentioned, we have $|\boldsymbol{d}_{pn_1}|\approx|\boldsymbol{d}_{Tn_1}|-\hat{\boldsymbol{d}}_{Tn_1}\cdot\boldsymbol{d}_{Tp}$, $|\boldsymbol{d}_{n_2q}|\approx|\boldsymbol{d}_{n_2R}|+\hat{\boldsymbol{d}}_{n_2R}\cdot\boldsymbol{d}_{Rq}$, $\langle\boldsymbol{v}_T,\boldsymbol{d}_{pn_1}\rangle\approx\langle\boldsymbol{v}_T,\boldsymbol{d}_{Tn_1}\rangle$, and $\langle\boldsymbol{v}_R,\boldsymbol{d}_{n_2q}\rangle\approx\langle\boldsymbol{v}_R,\boldsymbol{d}_{n_2R}\rangle$. With these approximations, we can obtain that

$$h_{pq}^{\mathrm{LoS}}(t)\approx e^{-j\frac{2\pi}{\lambda}\left(|\boldsymbol{d}_{TR}|+\hat{\boldsymbol{d}}_{TR}\cdot(-\boldsymbol{d}_{Tp}+\boldsymbol{d}_{Rq})\right)} e^{j2\pi(f_{T\max}\cos\langle\boldsymbol{v}_T,\boldsymbol{d}_{TR}\rangle-f_{R\max}\cos\langle\boldsymbol{v}_R,\boldsymbol{d}_{TR}\rangle)t} \quad (6)$$

$$h_{pq}^{\mathrm{SBT}}(t)\approx\lim_{N_1\to\infty}\frac{1}{\sqrt{N_1}}\sum_{n_1=1}^{N_1}e^{j\phi_{n_1}} e^{-j\frac{2\pi}{\lambda}\left(|\boldsymbol{d}_{Tn_1}|+|\boldsymbol{d}_{n_1R}|-\hat{\boldsymbol{d}}_{Tn_1}\cdot\boldsymbol{d}_{Tp}+\hat{\boldsymbol{d}}_{n_1R}\cdot\boldsymbol{d}_{Rq}\right)} e^{j2\pi(f_{T\max}\cos\langle\boldsymbol{v}_T,\boldsymbol{d}_{Tn_1}\rangle-f_{R\max}\cos\langle\boldsymbol{v}_R,\boldsymbol{d}_{n_1R}\rangle)t} \quad (7)$$

$$h_{pq}^{\mathrm{SBR}}(t)\approx\lim_{N_2\to\infty}\frac{1}{\sqrt{N_2}}\sum_{n_2=1}^{N_2}e^{j\phi_{n_2}} e^{-j\frac{2\pi}{\lambda}\left(|\boldsymbol{d}_{Tn_2}|+|\boldsymbol{d}_{n_2R}|-\hat{\boldsymbol{d}}_{Tn_2}\cdot\boldsymbol{d}_{Tp}+\hat{\boldsymbol{d}}_{n_2R}\cdot\boldsymbol{d}_{Rq}\right)} e^{j2\pi(f_{T\max}\cos\langle\boldsymbol{v}_T,\boldsymbol{d}_{Tn_2}\rangle-f_{R\max}\cos\langle\boldsymbol{v}_R,\boldsymbol{d}_{n_2R}\rangle)t} \quad (8)$$

$$h_{pq}^{\mathrm{DB}}(t)\approx\lim_{N_1,N_2\to\infty}\frac{1}{\sqrt{N_1N_2}}\sum_{n_1=1}^{N_1}\sum_{n_2=1}^{N_2}e^{j\phi_{n_1n_2}} e^{-j\frac{2\pi}{\lambda}\left(|\boldsymbol{d}_{Tn_1}|+|\boldsymbol{d}_{n_1n_2}|+|\boldsymbol{d}_{n_2R}|-\hat{\boldsymbol{d}}_{Tn_1}\cdot\boldsymbol{d}_{Tp}+\hat{\boldsymbol{d}}_{n_2R}\cdot\boldsymbol{d}_{Rq}\right)} e^{j2\pi(f_{T\max}\cos\langle\boldsymbol{v}_T,\boldsymbol{d}_{Tn_1}\rangle-f_{R\max}\cos\langle\boldsymbol{v}_R,\boldsymbol{d}_{n_2R}\rangle)t}. \quad (9)$$

The normalized ST-CF is defined by

$$R_{pq,p'q'}(\tau)=\frac{\mathbb{E}\left[h_{pq}(t)h_{p'q'}^*(t+\tau)\right]}{\sqrt{\mathbb{E}\left[|h_{pq}(t)|^2\right]\mathbb{E}\left[|h_{p'q'}(t)|^2\right]}} \quad (10)$$

and by substituting (1) into (10), we have

$$R_{pq,p'q'}(\tau)=\frac{K}{K+1}R_{pq,p'q'}^{\mathrm{LoS}}(\tau)+\frac{\eta_{\mathrm{SBT}}}{K+1}R_{pq,p'q'}^{\mathrm{SBT}}(\tau)+\frac{\eta_{\mathrm{SBR}}}{K+1}R_{pq,p'q'}^{\mathrm{SBR}}(\tau)+\frac{\eta_{\mathrm{DB}}}{K+1}R_{pq,p'q'}^{\mathrm{DB}}(\tau) \quad (11)$$

where the constituent ST-CFs are

$$R_{pq,p'q'}^{\mathrm{LoS}}(\tau)=e^{j\frac{2\pi}{\lambda}\hat{\boldsymbol{d}}_{TR}\cdot\left(-\boldsymbol{d}_{pp'}+\boldsymbol{d}_{qq'}\right)} e^{-j2\pi(f_{T\max}\cos\langle\boldsymbol{v}_T,\boldsymbol{d}_{TR}\rangle-f_{R\max}\cos\langle\boldsymbol{v}_R,\boldsymbol{d}_{TR}\rangle)\tau} \quad (12)$$

$$R_{pq,p'q'}^{\mathrm{SBT}}(\tau)=\lim_{N_1\to\infty}\frac{1}{N_1}\sum_{n_1=1}^{N_1}\mathbb{E}\left[e^{j\frac{2\pi}{\lambda}\left(-\hat{\boldsymbol{d}}_{Tn_1}\cdot\boldsymbol{d}_{pp'}+\hat{\boldsymbol{d}}_{n_1R}\cdot\boldsymbol{d}_{qq'}\right)} e^{-j2\pi(f_{T\max}\cos\langle\boldsymbol{v}_T,\boldsymbol{d}_{Tn_1}\rangle-f_{R\max}\cos\langle\boldsymbol{v}_R,\boldsymbol{d}_{n_1R}\rangle)\tau}\right] \quad (13)$$

$$R_{pq,p'q'}^{\mathrm{SBR}}(\tau)=\lim_{N_2\to\infty}\frac{1}{N_2}\sum_{n_2=1}^{N_2}\mathbb{E}\left[e^{j\frac{2\pi}{\lambda}\left(-\hat{\boldsymbol{d}}_{Tn_2}\cdot\boldsymbol{d}_{pp'}+\hat{\boldsymbol{d}}_{n_2R}\cdot\boldsymbol{d}_{qq'}\right)} e^{-j2\pi(f_{T\max}\cos\langle\boldsymbol{v}_T,\boldsymbol{d}_{Tn_2}\rangle-f_{R\max}\cos\langle\boldsymbol{v}_R,\boldsymbol{d}_{n_2R}\rangle)\tau}\right] \quad (14)$$

$$R_{pq,p'q'}^{\mathrm{DB}}(\tau)=\lim_{N_1,N_2\to\infty}\frac{1}{N_1N_2}\sum_{n_1=1}^{N_1}\sum_{n_2=1}^{N_2}\mathbb{E}\left[e^{j\frac{2\pi}{\lambda}\left(-\hat{\boldsymbol{d}}_{Tn_1}\cdot\boldsymbol{d}_{pp'}+\hat{\boldsymbol{d}}_{n_2R}\cdot\boldsymbol{d}_{qq'}\right)} e^{-j2\pi(f_{T\max}\cos\langle\boldsymbol{v}_T,\boldsymbol{d}_{Tn_1}\rangle-f_{R\max}\cos\langle\boldsymbol{v}_R,\boldsymbol{d}_{n_2R}\rangle)\tau}\right]. \quad (15)$$

Note that $\boldsymbol{d}_{pp'}$ and $\boldsymbol{d}_{qq'}$ are the displacements from $A_T^{(p)}$ to $A_T^{(p')}$ and from $A_R^{(q)}$ to $A_R^{(q')}$, respectively. Besides, the cosines wherein can be expressed as $\cos\langle \boldsymbol{v}_T, \boldsymbol{d}_{TR}\rangle = \hat{\boldsymbol{d}}_{TR}\cdot\boldsymbol{v}_T/|\boldsymbol{v}_T|$, $\cos\langle \boldsymbol{v}_R, \boldsymbol{d}_{TR}\rangle = \hat{\boldsymbol{d}}_{TR}\cdot\boldsymbol{v}_R/|\boldsymbol{v}_R|$, $\cos\langle \boldsymbol{v}_T, \boldsymbol{d}_{Tn_1}\rangle = \hat{\boldsymbol{d}}_{Tn_1}\cdot\boldsymbol{v}_T/|\boldsymbol{v}_T|$, $\cos\langle \boldsymbol{v}_R, \boldsymbol{d}_{n_1R}\rangle = \hat{\boldsymbol{d}}_{n_1R}\cdot\boldsymbol{v}_R/|\boldsymbol{v}_R|$, $\cos\langle \boldsymbol{v}_T, \boldsymbol{d}_{Tn_2}\rangle = \hat{\boldsymbol{d}}_{Tn_2}\cdot\boldsymbol{v}_T/|\boldsymbol{v}_T|$, and $\cos\langle \boldsymbol{v}_R, \boldsymbol{d}_{n_2R}\rangle = \hat{\boldsymbol{d}}_{n_2R}\cdot\boldsymbol{v}_R/|\boldsymbol{v}_R|$. Recall $f_{T\max} = |\boldsymbol{v}_T|/\lambda$ and $f_{R\max} = |\boldsymbol{v}_R|/\lambda$, and then rewrite

$$R_{pq,p'q'}^{\mathrm{LoS}}(\tau) = e^{j\frac{2\pi}{\lambda}\hat{\boldsymbol{d}}_{TR}\cdot\left(-\boldsymbol{d}_{pp'}+\boldsymbol{d}_{qq'}-(\boldsymbol{v}_T-\boldsymbol{v}_R)\tau\right)} \tag{16}$$

$$R_{pq,p'q'}^{\mathrm{SBT}}(\tau) = \lim_{N_1\to\infty}\frac{1}{N_1}\sum_{n_1=1}^{N_1} \mathbb{E}\left[e^{j\frac{2\pi}{\lambda}\left(-\hat{\boldsymbol{d}}_{Tn_1}\cdot\left(\boldsymbol{d}_{pp'}+\boldsymbol{v}_T\tau\right)+\hat{\boldsymbol{d}}_{n_1R}\cdot\left(\boldsymbol{d}_{qq'}+\boldsymbol{v}_R\tau\right)\right)}\right] \tag{17}$$

$$R_{pq,p'q'}^{\mathrm{SBR}}(\tau) = \lim_{N_2\to\infty}\frac{1}{N_2}\sum_{n_2=1}^{N_2} \mathbb{E}\left[e^{j\frac{2\pi}{\lambda}\left(-\hat{\boldsymbol{d}}_{Tn_2}\cdot\left(\boldsymbol{d}_{pp'}+\boldsymbol{v}_T\tau\right)+\hat{\boldsymbol{d}}_{n_2R}\cdot\left(\boldsymbol{d}_{qq'}+\boldsymbol{v}_R\tau\right)\right)}\right] \tag{18}$$

$$R_{pq,p'q'}^{\mathrm{DB}}(\tau) = \lim_{N_1,N_2\to\infty}\frac{1}{N_1N_2}\sum_{n_1=1}^{N_1}\sum_{n_2=1}^{N_2} \mathbb{E}\left[e^{j\frac{2\pi}{\lambda}\left(-\hat{\boldsymbol{d}}_{Tn_1}\cdot\left(\boldsymbol{d}_{pp'}+\boldsymbol{v}_T\tau\right)+\hat{\boldsymbol{d}}_{n_2R}\cdot\left(\boldsymbol{d}_{qq'}+\boldsymbol{v}_R\tau\right)\right)}\right]. \tag{19}$$

By now, we have obtained the result of $R_{pq,p'q'}^{\mathrm{LoS}}(\tau)$, but $R_{pq,p'q'}^{\mathrm{SBT}}(\tau)$, $R_{pq,p'q'}^{\mathrm{SBR}}(\tau)$, and $R_{pq,p'q'}^{\mathrm{DB}}(\tau)$ still need further derivations. For the DB rays, thanks to the independence between the AoDs and the AoAs, it is straightforward to express the unit vectors $\hat{\boldsymbol{d}}_{Tn_1}$ and $\hat{\boldsymbol{d}}_{n_2R}$, in coordinate notation, as functions of $\alpha_T^{(n_1)}$ and $\beta_T^{(n_1)}$ and of $\alpha_R^{(n_2)}$ and $\beta_R^{(n_2)}$, respectively: $\hat{\boldsymbol{d}}_{Tn_1} = [\cos\alpha_T^{(n_1)}\cos\beta_T^{(n_1)}, \sin\alpha_T^{(n_1)}\cos\beta_T^{(n_1)}, \sin\beta_T^{(n_1)}]^{\mathrm{T}}$ and $\hat{\boldsymbol{d}}_{n_2R} = -[\cos\alpha_R^{(n_2)}\cos\beta_R^{(n_2)}, \sin\alpha_R^{(n_2)}\cos\beta_R^{(n_2)}, \sin\beta_R^{(n_2)}]^{\mathrm{T}}$. As for the SBT rays and the SBR rays, the expressions of $\hat{\boldsymbol{d}}_{Tn_1}$ and $\hat{\boldsymbol{d}}_{n_2R}$ remain the same as above. The tricky part is to express $\hat{\boldsymbol{d}}_{Tn_2}$ and $\hat{\boldsymbol{d}}_{n_1R}$ as proper forms containing $\alpha_R^{(n_2)}$ and $\beta_R^{(n_2)}$ and of $\alpha_T^{(n_1)}$ and $\beta_T^{(n_1)}$, respectively.[1] Note that $\hat{\boldsymbol{d}}_{Tn_2} = \boldsymbol{d}_{Tn_2}/|\boldsymbol{d}_{Tn_2}| = (\boldsymbol{d}_{TR} - \boldsymbol{d}_{n_2R})|\boldsymbol{d}_{Tn_2}|^{-1}$, where $|\boldsymbol{d}_{Tn_2}|^{-1} \approx (|\boldsymbol{d}_{TR}|^2 - 2\boldsymbol{d}_{TR}\cdot\boldsymbol{d}_{n_2R})^{-(1/2)} \approx |\boldsymbol{d}_{TR}|^{-1} + (\boldsymbol{d}_{TR}/|\boldsymbol{d}_{TR}|^3)\cdot\boldsymbol{d}_{n_2R}$. This enables us to obtain that $\hat{\boldsymbol{d}}_{Tn_2} \approx \hat{\boldsymbol{d}}_{TR} - \Delta_{n_2}\hat{\boldsymbol{d}}_{n_2R} + \Delta_{n_2}(\hat{\boldsymbol{d}}_{TR}\cdot\hat{\boldsymbol{d}}_{n_2R})\hat{\boldsymbol{d}}_{TR} - \Delta_{n_2}^2(\hat{\boldsymbol{d}}_{TR}\cdot\hat{\boldsymbol{d}}_{n_2R})\hat{\boldsymbol{d}}_{n_2R}$, where we have introduced $\Delta_{n_2} = |\boldsymbol{d}_{n_2R}|/|\boldsymbol{d}_{TR}|$. Since $|\boldsymbol{d}_{n_2R}| = R_2/\cos\beta_R^{(n_2)} \ll |\boldsymbol{d}_{TR}|$, one can see that Δ_{n_2} is small, and that $\Delta_{n_2}^2$ is even much smaller. Therefore, by omitting the extremely small term that contains $\Delta_{n_2}^2$, we have

$$\hat{\boldsymbol{d}}_{Tn_2} \approx \hat{\boldsymbol{d}}_{TR} - \Delta_{n_2}\hat{\boldsymbol{d}}_{n_2R} + \Delta_{n_2}\left(\hat{\boldsymbol{d}}_{TR}\cdot\hat{\boldsymbol{d}}_{n_2R}\right)\hat{\boldsymbol{d}}_{TR} \tag{20}$$

[1]The following mathematical process is essentially the algebraic way to find the dependence of the AoDs on the AoAs for the SBR rays, as well as that of the AoAs on the AoDs for the SBT rays. Such a systematically foolproof procedure epitomizes the superiority of our spatial-vector-based method over the conventional geometric-relation-based one that demands strong spatial-thinking skills or even clever triangle-solving tricks.

where the expression of $\hat{\boldsymbol{d}}_{n_2R}$ has been given in this paragraph. Similarly, the unit vector $\hat{\boldsymbol{d}}_{n_1R}$ can be approximated into

$$\hat{\boldsymbol{d}}_{n_1R} \approx \hat{\boldsymbol{d}}_{TR} - \Delta_{n_1}\hat{\boldsymbol{d}}_{Tn_1} + \Delta_{n_1}\left(\hat{\boldsymbol{d}}_{TR}\cdot\hat{\boldsymbol{d}}_{Tn_1}\right)\hat{\boldsymbol{d}}_{TR} \tag{21}$$

where the coordinates of $\hat{\boldsymbol{d}}_{Tn_1}$ have also been specified before. Substitution of (21) and (20) into (17) and (18) yields

$$R_{pq,p'q'}^{\mathrm{SBT}}(\tau) = \lim_{N_1\to\infty}\frac{1}{N_1}\sum_{n_1=1}^{N_1} e^{j\frac{2\pi}{\lambda}\hat{\boldsymbol{d}}_{TR}\cdot\left(\boldsymbol{d}_{qq'}+\boldsymbol{v}_R\tau\right)} \cdot\mathbb{E}\left[e^{-j\frac{2\pi}{\lambda}\hat{\boldsymbol{d}}_{Tn_1}\cdot\left(\Delta_{n_1}\left(\boldsymbol{d}_{qq'}+\boldsymbol{v}_R\tau-\hat{\boldsymbol{d}}_{TR}\cdot\left(\boldsymbol{d}_{qq'}+\boldsymbol{v}_R\tau\right)\hat{\boldsymbol{d}}_{TR}\right)+\left(\boldsymbol{d}_{pp'}+\boldsymbol{v}_T\tau\right)\right)}\right] \tag{22}$$

$$R_{pq,p'q'}^{\mathrm{SBR}}(\tau) = \lim_{N_2\to\infty}\frac{1}{N_2}\sum_{n_2=1}^{N_2} e^{-j\frac{2\pi}{\lambda}\hat{\boldsymbol{d}}_{TR}\cdot\left(\boldsymbol{d}_{pp'}+\boldsymbol{v}_T\tau\right)} \cdot\mathbb{E}\left[e^{j\frac{2\pi}{\lambda}\hat{\boldsymbol{d}}_{n_2R}\cdot\left(\Delta_{n_2}\left(\boldsymbol{d}_{pp'}+\boldsymbol{v}_T\tau-\hat{\boldsymbol{d}}_{TR}\cdot\left(\boldsymbol{d}_{pp'}+\boldsymbol{v}_T\tau\right)\hat{\boldsymbol{d}}_{TR}\right)+\left(\boldsymbol{d}_{qq'}+\boldsymbol{v}_R\tau\right)\right)}\right]. \tag{23}$$

To facilitate derivations, we convert (19), (22), and (23) into functions explicitly of $\alpha_T^{(n_1)}$, $\beta_T^{(n_1)}$, $\alpha_R^{(n_2)}$, and $\beta_R^{(n_2)}$. Let $\hat{\boldsymbol{d}}_{TR} = [\hat{d}_{TR,x}, \hat{d}_{TR,y}, \hat{d}_{TR,z}]^{\mathrm{T}}$, $\boldsymbol{d}_{pp'} = [d_{pp',x}, d_{pp',y}, d_{pp',z}]^{\mathrm{T}}$, $\boldsymbol{d}_{qq'} = [d_{qq',x}, d_{qq',y}, d_{qq',z}]^{\mathrm{T}}$, $\boldsymbol{v}_T = [v_{T,x}, v_{T,y}, v_{T,z}]^{\mathrm{T}}$, and $\boldsymbol{v}_R = [v_{R,x}, v_{R,y}, v_{R,z}]^{\mathrm{T}}$, and thus we have

$$R_{pq,p'q'}^{\mathrm{SBT}}(\tau) = \lim_{N_1\to\infty}\frac{1}{N_1}\sum_{n_1=1}^{N_1} e^{j\frac{2\pi}{\lambda}\hat{\boldsymbol{d}}_{TR}\cdot\left(\boldsymbol{d}_{qq'}+\boldsymbol{v}_R\tau\right)} \cdot\mathbb{E}\left[e^{-j\frac{2\pi}{\lambda}D_{n_1,x}^{\mathrm{SBT}}\cos\alpha_T^{(n_1)}\cos\beta_T^{(n_1)}} e^{-j\frac{2\pi}{\lambda}D_{n_1,y}^{\mathrm{SBT}}\sin\alpha_T^{(n_1)}\cos\beta_T^{(n_1)}} e^{-j\frac{2\pi}{\lambda}D_{n_1,z}^{\mathrm{SBT}}\sin\beta_T^{(n_1)}}\right] \tag{24}$$

$$R_{pq,p'q'}^{\mathrm{SBR}}(\tau) = \lim_{N_2\to\infty}\frac{1}{N_2}\sum_{n_2=1}^{N_2} e^{-j\frac{2\pi}{\lambda}\hat{\boldsymbol{d}}_{TR}\cdot\left(\boldsymbol{d}_{pp'}+\boldsymbol{v}_T\tau\right)} \cdot\mathbb{E}\left[e^{-j\frac{2\pi}{\lambda}D_{n_2,x}^{\mathrm{SBR}}\cos\alpha_R^{(n_2)}\cos\beta_R^{(n_2)}} e^{-j\frac{2\pi}{\lambda}D_{n_2,y}^{\mathrm{SBR}}\sin\alpha_R^{(n_2)}\cos\beta_R^{(n_2)}} e^{-j\frac{2\pi}{\lambda}D_{n_2,z}^{\mathrm{SBR}}\sin\beta_R^{(n_2)}}\right] \tag{25}$$

$$\begin{aligned} R_{pq,p'q'}^{\mathrm{DB}}(\tau) = \lim_{N_1,N_2\to\infty}\frac{1}{N_1N_2}\sum_{n_1=1}^{N_1}\sum_{n_2=1}^{N_2} \mathbb{E}\Big[& e^{-j\frac{2\pi}{\lambda}\left(d_{pp',x}+v_{T,x}\tau\right)\cos\alpha_T^{(n_1)}\cos\beta_T^{(n_1)}} \\ & e^{-j\frac{2\pi}{\lambda}\left(d_{pp',y}+v_{T,y}\tau\right)\sin\alpha_T^{(n_1)}\cos\beta_T^{(n_1)}} \\ & e^{-j\frac{2\pi}{\lambda}\left(d_{pp',z}+v_{T,z}\tau\right)\sin\beta_T^{(n_1)}} \\ & e^{-j\frac{2\pi}{\lambda}\left(d_{qq',x}+v_{R,x}\tau\right)\cos\alpha_R^{(n_2)}\cos\beta_R^{(n_2)}} \\ & e^{-j\frac{2\pi}{\lambda}\left(d_{qq',y}+v_{R,y}\tau\right)\sin\alpha_R^{(n_2)}\cos\beta_R^{(n_2)}} \\ & e^{-j\frac{2\pi}{\lambda}\left(d_{qq',z}+v_{R,z}\tau\right)\sin\beta_R^{(n_2)}}\Big] \end{aligned} \tag{26}$$

where $D^{\mathrm{SBT}}_{n_1,x/y/z}$ and $D^{\mathrm{SBR}}_{n_2,x/y/z}$ are, respectively, $D^{\mathrm{SBT}}_{n_1,x/y/z} = \Delta_{n_1}(d_{qq',x/y/z} + v_{R,x/y/z}\tau - \hat{\boldsymbol{d}}_{TR} \cdot (\boldsymbol{d}_{qq'} + \boldsymbol{v}_R\tau)\hat{d}_{TR,x/y/z}) + d_{pp',x/y/z} + v_{T,x/y/z}\tau$ and $D^{\mathrm{SBR}}_{n_2,x/y/z} = \Delta_{n_2}(d_{pp',x/y/z} + v_{T,x/y/z}\tau - \hat{\boldsymbol{d}}_{TR} \cdot (\boldsymbol{d}_{pp'} + \boldsymbol{v}_T\tau)\hat{d}_{TR,x/y/z}) + d_{qq',x/y/z} + v_{R,x/y/z}\tau$.

Since the number of local scatterers is infinite in this reference model, the discrete random variables $\alpha_T^{(n_1)}$, $\beta_T^{(n_1)}$, $\alpha_R^{(n_2)}$, and $\beta_R^{(n_2)}$ may be replaced by continuous ones α_T, β_T, α_R, and β_R. We assume these angles are independent with each other and use $f(\alpha_T)$, $f(\beta_T)$, $f(\alpha_R)$, and $f(\beta_R)$ to denote their marginal probability density functions (PDFs), respectively. In this article, we adopt the widely used von Mises PDF to characterize the azimuth AoD α_T and the azimuth AoA α_R, as given by $f(\alpha_T) = ([e^{k_T \cos(\alpha_T - \alpha_{T\mu})}]/[2\pi I_0(k_T)])$, $-\pi < \alpha_T \le \pi$ and $f(\alpha_R) = ([e^{k_R \cos(\alpha_R - \alpha_{R\mu})}]/[2\pi I_0(k_R)])$, $-\pi < \alpha_R \le \pi$, where $I_0(\cdot)$ is the zeroth order Bessel function of the first kind, $\alpha_{T\mu}$ and $\alpha_{R\mu}$ are the mean angles at which the scatterers are projected to the horizontal plane, and the nonnegative parameters k_T and k_R control the spreads of scatterers around the mean values. The elevation AoA and elevation AoD are described by the cosine PDF as $f(\beta_T) = (\pi/4\beta_{Tm})\cos([\pi/2][\beta_T - \beta_{T\mu}]/\beta_{Tm})$, $|\beta_T - \beta_{T\mu}| \le \beta_{Tm}$ and $f(\beta_R) = (\pi/4\beta_{Rm})\cos([\pi/2][\beta_R - \beta_{R\mu}]/\beta_{Rm})$, $|\beta_R - \beta_{R\mu}| \le \beta_{Rm}$, where $\beta_{T\mu}$ and $\beta_{R\mu}$ represent the mean values, and the nonnegative parameters β_{Tm} and β_{Rm} control the spreads. For conciseness, define $\beta_{T\mu} - \beta_{Tm} = \beta_{T\min}$, $\beta_{T\mu} + \beta_{Tm} = \beta_{T\max}$, $\beta_{R\mu} - \beta_{Rm} = \beta_{R\min}$, and $\beta_{R\mu} + \beta_{Rm} = \beta_{R\max}$. Then with the new definitions $D^{\mathrm{SBT}}_{x/y/z} = \Delta_T(d_{qq',x/y/z} + v_{R,x/y/z}\tau - \hat{\boldsymbol{d}}_{TR} \cdot (\boldsymbol{d}_{qq'} + \boldsymbol{v}_R\tau)\hat{d}_{TR,x/y/z}) + d_{pp',x/y/z} + v_{T,x/y/z}\tau$ and $D^{\mathrm{SBR}}_{x/y/z} = \Delta_R(d_{pp',x/y/z} + v_{T,x/y/z}\tau - \hat{\boldsymbol{d}}_{TR} \cdot (\boldsymbol{d}_{pp'} + \boldsymbol{v}_T\tau)\hat{d}_{TR,x/y/z}) + d_{qq',x/y/z} + v_{R,x/y/z}\tau$, where $\Delta_T = R_1/\cos\beta_T/|\boldsymbol{d}_{TR}|$ and $\Delta_R = R_2/\cos\beta_R/|\boldsymbol{d}_{TR}|$, the summations as in (24)–(26) become the integrals

$$R^{\mathrm{SBT}}_{pq,p'q'}(\tau) = e^{j\frac{2\pi}{\lambda}\hat{\boldsymbol{d}}_{TR}\cdot\left(\boldsymbol{d}_{qq'}+\boldsymbol{v}_R\tau\right)} \int_{\beta_{T\min}}^{\beta_{T\max}} \int_{-\pi}^{\pi} f(\alpha_T) f(\beta_T) e^{-j\frac{2\pi}{\lambda}D_x^{\mathrm{SBT}}\cos\alpha_T\cos\beta_T} e^{-j\frac{2\pi}{\lambda}D_y^{\mathrm{SBT}}\sin\alpha_R\cos\beta_R} e^{-j\frac{2\pi}{\lambda}D_z^{\mathrm{SBT}}\sin\beta_T} \mathrm{d}\alpha_T \mathrm{d}\beta_T \tag{27}$$

$$R^{\mathrm{SBR}}_{pq,p'q'}(\tau) = e^{-j\frac{2\pi}{\lambda}\hat{\boldsymbol{d}}_{TR}\cdot\left(\boldsymbol{d}_{pp'}+\boldsymbol{v}_T\tau\right)} \int_{\beta_{R\min}}^{\beta_{R\max}} \int_{-\pi}^{\pi} f(\alpha_R) f(\beta_R) e^{-j\frac{2\pi}{\lambda}D_x^{\mathrm{SBR}}\cos\alpha_R\cos\beta_R} e^{-j\frac{2\pi}{\lambda}D_y^{\mathrm{SBR}}\sin\alpha_R\cos\beta_R} e^{-j\frac{2\pi}{\lambda}D_z^{\mathrm{SBR}}\sin\beta_R} \mathrm{d}\alpha_R \mathrm{d}\beta_R \tag{28}$$

$$\begin{aligned} R^{\mathrm{DB}}_{pq,p'q'}(\tau) = &\int_{\beta_{R\min}}^{\beta_{R\max}} \int_{-\pi}^{\pi} \int_{\beta_{T\min}}^{\beta_{T\max}} \int_{-\pi}^{\pi} f(\alpha_T) f(\beta_T) \\ & f(\alpha_R) f(\beta_R) e^{-j\frac{2\pi}{\lambda}\left(d_{pp',x}+v_{T,x}\tau\right)\cos\alpha_T\cos\beta_T} \\ & e^{-j\frac{2\pi}{\lambda}\left(d_{pp',y}+v_{T,y}\tau\right)\sin\alpha_T\cos\beta_T} \\ & e^{-j\frac{2\pi}{\lambda}\left(d_{pp',z}+v_{T,z}\tau\right)\sin\beta_T} \\ & e^{-j\frac{2\pi}{\lambda}\left(d_{qq',x}+v_{R,x}\tau\right)\cos\alpha_R\cos\beta_R} \\ & e^{-j\frac{2\pi}{\lambda}\left(d_{qq',y}+v_{R,y}\tau\right)\sin\alpha_R\cos\beta_R} \\ & e^{-j\frac{2\pi}{\lambda}\left(d_{qq',z}+v_{R,z}\tau\right)\sin\beta_R} \mathrm{d}\alpha_T \mathrm{d}\beta_T \mathrm{d}\alpha_R \mathrm{d}\beta_R. \end{aligned} \tag{29}$$

Using the equality $\int_{-\pi}^{\pi} e^{a\sin c + b\cos c}\mathrm{d}c = 2\pi I_0(\sqrt{a^2+b^2})$ [43, Eq. (3.338-4)], we can solve the integral with respect to α_T or with respect to α_R in (27) and (28) as $R^{\mathrm{SBT}}_{pq,p'q'}(\tau) = e^{j(2\pi/\lambda)\hat{\boldsymbol{d}}_{TR}\cdot(\boldsymbol{d}_{qq'}+\boldsymbol{v}_R\tau)} \cdot \int_{\beta_{T\min}}^{\beta_{T\max}} e^{-j(2\pi/\lambda)D_z^{\mathrm{SBT}}\sin\beta_T} \cdot [(\pi\cos([\pi/2][\beta_T - \beta_{T\mu}/\beta_{Tm}]))/4\beta_{Tm}] \cdot ([I_0(\sqrt{X_{\mathrm{SBT}}^2 + Y_{\mathrm{SBT}}^2})]/I_0(k_T))\mathrm{d}\beta_T$ and $R^{\mathrm{SBR}}_{pq,p'q'}(\tau) = e^{-j(2\pi/\lambda)\hat{\boldsymbol{d}}_{TR}\cdot(\boldsymbol{d}_{pp'}+\boldsymbol{v}_T\tau)} \cdot \int_{\beta_{R\min}}^{\beta_{R\max}} e^{-j(2\pi/\lambda)D_z^{\mathrm{SBR}}\sin\beta_R} \cdot ([\pi\cos([\pi/2][\beta_R - \beta_{R\mu}]/\beta_{Rm})]/4\beta_{Rm}) \cdot ([I_0(\sqrt{X_{\mathrm{SBR}}^2 + Y_{\mathrm{SBR}}^2})]/I_0(k_R))\mathrm{d}\beta_R$, where $X_{\mathrm{SBT}} = -j(2\pi/\lambda)D_x^{\mathrm{SBT}}\cos\beta_T + k_T\cos\alpha_{T\mu}$, $Y_{\mathrm{SBT}} = -j(2\pi/\lambda) D_y^{\mathrm{SBT}}\cos\beta_T + k_T\sin\alpha_{T\mu}$, $X_{\mathrm{SBR}} = -j(2\pi/\lambda) D_x^{\mathrm{SBR}}\cos\beta_R + k_R\cos\alpha_{R\mu}$, and $Y_{\mathrm{SBR}} = -j(2\pi/\lambda)D_y^{\mathrm{SBR}}\cos\beta_R + k_R\sin\alpha_{R\mu}$. Similarly, in (29), the integrals with respect to α_T and α_R can be solved into $R^{\mathrm{DB}}_{pq,p'q'}(\tau) = \int_{\beta_{T\min}}^{\beta_{T\max}} e^{-j(2\pi/\lambda)(d_{pp',z}+v_{T,z}\tau)\sin\beta_T} \cdot ([I_0(\sqrt{X_{\mathrm{DB}}^2 + Y_{\mathrm{DB}}^2})]/I_0(k_T)) \cdot ([\pi\cos([\pi/2][(\beta_T - \beta_{T\mu})/\beta_{Tm}])]/4\beta_{Tm})\mathrm{d}\beta_T \cdot \int_{\beta_{R\min}}^{\beta_{R\max}}([\pi \cos([\pi/2][(\beta_R - \beta_{R\mu})/\beta_{Rm}])]/4\beta_{Rm}) \cdot e^{-j(2\pi/\lambda)(d_{qq',z}+v_{R,z}\tau)\sin\beta_R} \cdot ([I_0(\sqrt{Z_{\mathrm{DB}}^2 + W_{\mathrm{DB}}^2})]/I_0(k_R))\mathrm{d}\beta_R$, where the parameters are defined as $X_{\mathrm{DB}} = -j(2\pi/\lambda)(d_{pp',x} + v_{T,x}\tau)\cos\beta_T + k_T\cos\alpha_{T\mu}$, $Y_{\mathrm{DB}} = -j(2\pi/\lambda)(d_{pp',y} + v_{T,y}\tau)\cos\beta_T + k_T\sin\alpha_{T\mu}$, $Z_{\mathrm{DB}} = -j(2\pi/\lambda)(d_{qq',x} + v_{R,x}\tau)\cos\beta_R + k_R\cos\alpha_{R\mu}$, and $W_{\mathrm{DB}} = -j(2\pi/\lambda)(d_{qq',y} + v_{R,y}\tau)\cos\beta_R + k_R\sin\alpha_{R\mu}$.

Unfortunately, the existence of β_T or β_R in these parameters makes it almost impossible to solve the remaining integrals with respect to β_T and β_R. Note that it has been analytically demonstrated that the spreads of these elevation angles typically do not exceed 0.5 rad $\approx 30°$ [44], which inspires us to make a small-elevation-angular-spread assumption, i.e., $\beta_{Tm}, \beta_{Rm} \le 30°/2 = 15°$. This gives us the following Taylor approximations: $\cos\beta_T \approx \cos\beta_{T\mu}$, $\sin\beta_T \approx \sin\beta_{T\mu} + (\beta_T - \beta_{T\mu})\cos\beta_{T\mu}$, $\cos\beta_R \approx \cos\beta_{R\mu}$, and $\sin\beta_R \approx \sin\beta_{R\mu} + (\beta_R - \beta_{R\mu})\cos\beta_{R\mu}$, and, thereby, allows us to solve the three constituent ST-CFs as

$$R^{\mathrm{SBT}}_{pq,p'q'}(\tau) = e^{j\frac{2\pi}{\lambda}\hat{\boldsymbol{d}}_{TR}\cdot\left(\boldsymbol{d}_{qq'}+\boldsymbol{v}_R\tau\right)} \frac{I_0\left(\sqrt{\tilde{X}_{\mathrm{SBT}}^2 + \tilde{Y}_{\mathrm{SBT}}^2}\right)}{I_0(k_T)} e^{-j\frac{2\pi}{\lambda}\tilde{D}_z^{\mathrm{SBT}}\sin\beta_{T\mu}} \frac{\cos\left(\frac{2\pi\beta_{Tm}}{\lambda}\tilde{D}_z^{\mathrm{SBT}}\cos\beta_{T\mu}\right)}{1 - \left(\frac{4\beta_{Tm}}{\lambda}\tilde{D}_z^{\mathrm{SBT}}\cos\beta_{T\mu}\right)^2} \tag{30}$$

$$R^{\mathrm{SBR}}_{pq,p'q'}(\tau) = e^{-j\frac{2\pi}{\lambda}\hat{\boldsymbol{d}}_{TR}\cdot\left(\boldsymbol{d}_{pp'}+\boldsymbol{v}_T\tau\right)} \frac{I_0\left(\sqrt{\tilde{X}_{\mathrm{SBR}}^2 + \tilde{Y}_{\mathrm{SBR}}^2}\right)}{I_0(k_R)} e^{-j\frac{2\pi}{\lambda}\tilde{D}_z^{\mathrm{SBR}}\sin\beta_{R\mu}} \frac{\cos\left(\frac{2\pi\beta_{Rm}}{\lambda}\tilde{D}_z^{\mathrm{SBR}}\cos\beta_{R\mu}\right)}{1 - \left(\frac{4\beta_{Rm}}{\lambda}\tilde{D}_z^{\mathrm{SBR}}\cos\beta_{R\mu}\right)^2} \tag{31}$$

$$R^{\mathrm{DB}}_{pq,p'q'}(\tau) \approx \frac{I_0\left(\sqrt{\tilde{X}_{\mathrm{DB}}^2 + \tilde{Y}_{\mathrm{DB}}^2}\right)}{I_0(k_T)} e^{-j\frac{2\pi}{\lambda}\left(d_{pp',z}+v_{T,z}\tau\right)\sin\beta_{T\mu}} \frac{\cos\left(\frac{2\pi}{\lambda}\beta_{Tm}\left(d_{pp',z}+v_{T,z}\tau\right)\cos\beta_{T\mu}\right)}{1 - \left(\frac{4\beta_{Tm}\left(d_{pp',z}+v_{T,z}\tau\right)\cos\beta_{T\mu}}{\lambda}\right)^2}$$

$$\frac{I_0\left(\sqrt{\tilde{Z}_{\mathrm{DB}}^2+\tilde{W}_{\mathrm{DB}}^2}\right)}{I_0(k_R)}e^{-j\frac{2\pi}{\lambda}\left(d_{qq',z}+v_{R,z}\tau\right)\sin\beta_{R\mu}}$$
$$\frac{\cos\left(\frac{2\pi}{\lambda}\beta_{Rm}\left(d_{qq',z}+v_{R,z}\tau\right)\cos\beta_{R\mu}\right)}{1-\left(\frac{4\beta_{Rm}\left(d_{qq',z}+v_{R,z}\tau\right)\cos\beta_{R\mu}}{\lambda}\right)^2} \tag{32}$$

where the approximated parameters with tildes overhead are

$$\tilde{X}_{\mathrm{SBT}}=-j\frac{2\pi}{\lambda}\tilde{D}_x^{\mathrm{SBT}}\cos\beta_{T\mu}+k_T\cos\alpha_{T\mu} \tag{33}$$
$$\tilde{Y}_{\mathrm{SBT}}=-j\frac{2\pi}{\lambda}\tilde{D}_y^{\mathrm{SBT}}\cos\beta_{T\mu}+k_T\sin\alpha_{T\mu} \tag{34}$$
$$\tilde{X}_{\mathrm{SBR}}=-j\frac{2\pi}{\lambda}\tilde{D}_x^{\mathrm{SBR}}\cos\beta_{R\mu}+k_R\cos\alpha_{R\mu} \tag{35}$$
$$\tilde{Y}_{\mathrm{SBR}}=-j\frac{2\pi}{\lambda}\tilde{D}_y^{\mathrm{SBR}}\cos\beta_{R\mu}+k_R\sin\alpha_{R\mu} \tag{36}$$
$$\tilde{X}_{\mathrm{DB}}=-j\frac{2\pi}{\lambda}\left(d_{pp',x}+v_{T,x}\tau\right)\cos\beta_{T\mu}+k_T\cos\alpha_{T\mu} \tag{37}$$
$$\tilde{Y}_{\mathrm{DB}}=-j\frac{2\pi}{\lambda}\left(d_{pp',y}+v_{T,y}\tau\right)\cos\beta_{T\mu}+k_T\sin\alpha_{T\mu} \tag{38}$$
$$\tilde{Z}_{\mathrm{DB}}=-j\frac{2\pi}{\lambda}\left(d_{qq',x}+v_{R,x}\tau\right)\cos\beta_{R\mu}+k_R\cos\alpha_{R\mu} \tag{39}$$
$$\tilde{W}_{\mathrm{DB}}=-j\frac{2\pi}{\lambda}\left(d_{qq',y}+v_{R,y}\tau\right)\cos\beta_{R\mu}+k_R\sin\alpha_{R\mu}. \tag{40}$$

Besides, the parameters $\tilde{D}_{x/y/z}^{\mathrm{SBT}}$ and $\tilde{D}_{x/y/z}^{\mathrm{SBR}}$ are defined as, respectively, $\tilde{D}_{x/y/z}^{\mathrm{SBT}}=\tilde{\Delta}_T(d_{qq',x/y/z}+v_{R,x/y/z}\tau-\hat{\boldsymbol{d}}_{TR}\cdot(\boldsymbol{d}_{qq'}+\boldsymbol{v}_R\tau)\hat{d}_{TR,x/y/z})+d_{pp',x/y/z}+v_{T,x/y/z}\tau$ and $\tilde{D}_{x/y/z}^{\mathrm{SBR}}=\tilde{\Delta}_R(d_{pp',x/y/z}+v_{T,x/y/z}\tau-\hat{\boldsymbol{d}}_{TR}\cdot(\boldsymbol{d}_{pp'}+\boldsymbol{v}_T\tau)\hat{d}_{TR,x/y/z})+d_{qq',x/y/z}+v_{R,x/y/z}\tau$, where $\tilde{\Delta}_T=R_1/\cos\beta_{T\mu}/|\boldsymbol{d}_{TR}|$ and $\tilde{\Delta}_R=R_2/\cos\beta_{R\mu}/|\boldsymbol{d}_{TR}|$, respectively.

It should be noted that the velocities $\boldsymbol{v}_T$ and $\boldsymbol{v}_R$ can be expanded as [45]

$$\boldsymbol{v}_T=v_T\left[\cos\gamma_T\cos\xi_T,\sin\gamma_T\cos\xi_T,\sin\xi_T\right]^{\mathrm{T}} \tag{41}$$
$$\boldsymbol{v}_R=v_R\left[\cos\gamma_R\cos\xi_R,\sin\gamma_R\cos\xi_R,\sin\xi_R\right]^{\mathrm{T}} \tag{42}$$

where $v_T=|\boldsymbol{v}_T|$ and $v_R=|\boldsymbol{v}_R|$ are the speeds of the two UAV stations, respectively. Besides, the displacements $\boldsymbol{d}_{pp'}$ and $\boldsymbol{d}_{qq'}$ (under ULA configuration) can be specified as [46]

$$\boldsymbol{d}_{pp'}=(p-p')d_T\left[\cos\theta_T\cos\psi_T,\sin\theta_T\cos\psi_T,\sin\psi_T\right]^{\mathrm{T}} \tag{43}$$
$$\boldsymbol{d}_{qq'}=(q-q')d_R\left[\cos\theta_R\cos\psi_R,\sin\theta_R\cos\psi_R,\sin\psi_R\right]^{\mathrm{T}}. \tag{44}$$

Worth pointing out is that, although the ULA configuration is used throughout this article, it is not difficult to extend to some other antenna configurations, e.g., uniform circular array and uniform spherical array. Interested readers are referred to [29] for details on the mathematical representations of the antenna elements in those two configurations.

Substituting (16) and (30)–(32) into (11), we finally arrive at a closed-form ST-CF that jointly considers the LoS, the SBT, the SBR, and the DB rays. It can be easily observed that:

1) $R_{pq,p'q'}^{\mathrm{LoS}}(\tau)$, $R_{pq,p'q'}^{\mathrm{SBT}}(\tau)$, and $R_{pq,p'q'}^{\mathrm{SBR}}(\tau)$ all depend on the unit vector $\hat{\boldsymbol{d}}_{TR}$, while $R_{pq,p'q'}^{\mathrm{DB}}(\tau)$ does not. This indicates that the relative location or direction between the Tx and Rx is irrelevant to the correlations of the DB rays but is significant to the LoS, SBT, and SBR cases;
2) $R_{pq,p'q'}^{\mathrm{LoS}}(\tau)$ is independent of the radii of the two imaginary cylinders, which is obvious. In contrast, $R_{pq,p'q'}^{\mathrm{SBT}}(\tau)$ is dependent on the radius of the imaginary cylinder at the Tx side only, and $R_{pq,p'q'}^{\mathrm{SBR}}(\tau)$ is dependent on the radius of the imaginary cylinder at the Rx side only. Besides, $R_{pq,p'q'}^{\mathrm{DB}}(\tau)$ is dependent on the radii of both the cylinder at the Tx side and Rx side;
3) $R_{pq,p'q'}^{\mathrm{SBT}}(\tau)$ and $R_{pq,p'q'}^{\mathrm{SBR}}(\tau)$ have analogous expressions. More specifically, the expression of $R_{pq,p'q'}^{\mathrm{SBT}}(\tau)$ can be obtained from that of $R_{pq,p'q'}^{\mathrm{SBR}}(\tau)$ by replacing the subscripts $_{pp'}$ with $_{qq'}$, $_R$ with $_T$, and $_{TR}$ with $_{RT}$. Interestingly, this is the very operation that interchanges the Tx and Rx, which turns the SBR case into the SBT case.

To exemplify the validity of the approximate expressions (31) and (32), we show in Fig. 2 that the closed-form approximate results generally agree with the numerical exact ones. The results in Fig. 2 are obtained under the parameters $M_T=M_R=2$, $\boldsymbol{d}_{TR}=[0, 50\text{ m}, -50\text{ m}]^{\mathrm{T}}$, $R_1=R_2=2$ m, $v_T=v_R=1$ m/s, $\gamma_T=20°$, $\gamma_R=40°$, $\xi_T=\xi_R=0°$, $d_T=d_R=0.5\lambda$, $\theta_T=\theta_R=45°$, $\psi_T=\psi_R=120°$, $k_T=k_R=20$, $\alpha_{T\mu}=70°$, $\alpha_{R\mu}=20°$, and $\beta_{T\mu}=\beta_{R\mu}=10°$. Apart from the close approximation under small β_m, the closed-form expressions have much shorter computation time than the numerically obtained exact ones, which indicates the utility and the superiority of the derived ST-CF.

Many existing correlation functions are special cases of the suggested closed-form ST-CF as in (11) with (16) and (30)–(32), as are summarized in Tables II and III. Specifically, Table II lists some correlation functions previously obtained from the one-ring or the one-cylinder model, and Table III enumerates several correlation functions previously obtained from the two-ring or the two-cylinder model. These existing correlation functions can be reached by simplifying the ST-CF of ours with the specific condition as in each entry of the tables, which shows the high generality of the derived ST-CF.

To demonstrate the utility of the proposed ST-CF in realistic scenarios, we compare some measured A2A Doppler PSDs reported in [47] to the theoretical ones. Although the two measurement aircraft used in [47] were human-piloted planes, the results wherein can be seen as what we would expect using large-size fixed-wing UAVs. Note that the space-Doppler PSD is defined as the Fourier transform of the ST-CF, which can be written as $S_{pq,p'q'}(f_D)=\mathcal{F}\{R_{pq,p'q'}(\tau)\}=\int_{-\infty}^{\infty}R_{pq,p'q'}(\tau)e^{-j2\pi f_D\tau}\mathrm{d}\tau$. The comparison is presented in Fig. 3. In Fig. 3(a), the measured results are taken from [47, Fig. 8 (Urban)] and the theoretical ones are obtained under $M_T=M_R=1$, $p=p'=1$, $q=q'=1$, $f_c=250$ MHz, $f_{T\max}=f_{R\max}=80$ Hz, $\gamma_T=\gamma_R=90°$, $\xi_T=\xi_R=0°$, $\boldsymbol{d}_{TR}=[0, 2000\text{ m}, 1600\text{ m}-1600\text{ m}]^{\mathrm{T}}=[0, 2000\text{ m}, 0]^{\mathrm{T}}$, $R_1=R_2=8$ m, $k_T=k_R=10$, $\alpha_{T\mu}=90°$, $\alpha_{R\mu}=270°$, $\beta_{Tm}=\beta_{Rm}=15°$, and $\beta_{T\mu}=\beta_{R\mu}=-30°$, $K=7$, $\eta_{\mathrm{SBT}}=\eta_{\mathrm{SBR}}=0.3$, and $\eta_{\mathrm{DB}}=0.4$. In Fig. 3(b), the measured results are taken from [47, Fig. 8 (Grassland)] and the theoretical ones

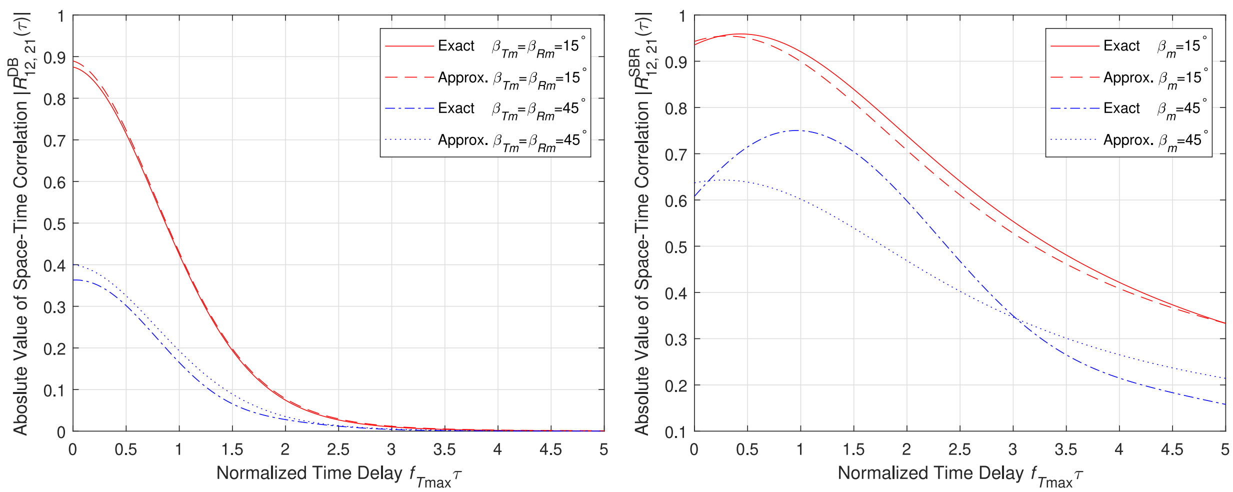

(a) (b)

Fig. 2. Comparison of the absolute value between the approximate (approx.) ST-CF and the exact one for (a) DB case and (b) SB(R) case. Every curve in (a) and (b) consists of 500 valid points. In order of the captions from top to bottom, the computation time for each curve in (a) is 0.005041, 1707.612227, 0.002176, and 1355.606072 s, respectively, and the computation time for each curve in (b) is 0.004608, 0.693944, 0.001422, and 0.678453 s, respectively, on a desktop PC.

TABLE II
SOME CORRELATION FUNCTIONS OBTAINED FROM THE ONE-RING AND THE ONE-CYLINDER MODEL THAT ARE SPECIAL CASES OF THE ST-CF DERIVED IN THIS ARTICLE. NOTE THAT THE EXPRESSIONS LISTED IN THE TABLE ARE OBTAINED UNDER THE RELATIVE LOCATION BETWEEN THE TX AND RX GIVEN BY $\boldsymbol{d}_{TR} = [D, 0, 0]^{\mathrm{T}}$. (SISO: SINGLE-INPUT SINGLE-OUTPUT, SIMO: SINGLE-INPUT MULTIPLE-OUTPUT, $J_0(\cdot)$: THE ZEROTH-ORDER BESSEL FUNCTION OF THE FIRST KIND)

Ref.	Expression	Description	Condition
[37]	$J_0\left(2\pi f_{R\max}\tau\right)$, from a 2-D one-ring model.	SBR rays only, fixed Tx, 2-D mobile Rx, SISO, 2-D isotropic scattering.	$K=0$, $\eta_{\mathrm{SBT}}=0$, $\eta_{\mathrm{DB}}=0$, $v_T=0$, $\xi_R=0$, $d_T=d_R=0$, $k_T=k_R=0$, $\beta_{Tm}=\beta_{Rm}=0$.
[38]	$J_0\left(\frac{2\pi}{\lambda}d_R\right)$, from a 2-D one-ring model.	SBR rays only, fixed Tx and Rx, 2-D SIMO, 2-D isotropic scattering.	$K=0$, $\eta_{\mathrm{SBT}}=0$, $\eta_{\mathrm{DB}}=0$, $v_T=v_R=0$, $d_T=0$, $\psi_R=0$, $k_T=k_R=0$, $\beta_{Tm}=\beta_{Rm}=0$.
[26]	$J_0\left(\Delta\frac{2\pi}{\lambda}d_T\right)$, from a 2-D one-ring model.	SBR rays only, fixed Tx and Rx, 2-D MISO, 2-D isotropic scattering.	$K=0$, $\eta_{\mathrm{SBT}}=0$, $\eta_{\mathrm{DB}}=0$, $v_T=v_R=0$, $d_R=0$, $\psi_T=0$, $k_T=k_R=0$, $\beta_{Tm}=\beta_{Rm}=0$.
[27]	$\frac{K}{K+1}e^{j\frac{2\pi}{\lambda}(d_T\cos\theta_T-d_R\cos\theta_R)}e^{j2\pi f_{R\max}\tau\cos\gamma_R}$ $+\frac{1}{K+1}e^{j2\frac{2\pi}{\lambda}d_T\cos\theta_T}\frac{I_0\left(\sqrt{x^2+y^2}\right)}{I_0(k_R)}$, where $x=j\frac{2\pi}{\lambda}d_R\cos\theta_R-j2\pi f_{R\max}\tau\cos\gamma_R+k_R\cos\alpha_{R\mu}$ and $y=j\Delta\frac{2\pi}{\lambda}d_T\sin\theta_T$ $+j\frac{2\pi}{\lambda}d_R\sin\theta_R-j2\pi f_{R\max}\tau\sin\gamma_R+k_R\sin\alpha_{R\mu}$, $(\Delta\approx R_2/D)$ from a 2-D one-ring model.	LoS and SBR rays only, fixed Tx, 2-D mobile Rx, 2-D MIMO, 2-D non-isotropic scattering.	$\eta_{\mathrm{SBT}}=0$, $\eta_{\mathrm{DB}}=0$, $v_T=0$, $\xi_R=0$, $\psi_T=\psi_R=0$, $k_T=0$, $\beta_{Tm}=\beta_{Rm}=0$.
[39]	$\exp\left\{j\frac{2\pi}{\lambda}d_T\sin\theta_T\cos\psi_T\right\}I_0\left(\sqrt{x^2+y^2}\right)$ $\frac{\cos\left(\frac{2\pi}{\pi}\beta_m d_R\sin\psi_R\right)}{1-\left(\frac{4\beta_m}{\lambda}d_R\sin\psi_R\right)^2}$, where $x=j\frac{2\pi}{\lambda}\Delta d_T\cos\theta_T\cos\psi_T$ $+j\frac{2\pi}{\lambda}d_R\cos\theta_R\cos\psi_R-j2\pi f_{R\max}\tau\cos\gamma_R$, and $y=j\frac{2\pi}{\lambda}d_R\sin\theta_R\cos\psi_R-j2\pi f_{R\max}\tau\sin\gamma_R$, $(\Delta\approx R_2/D$ if $R,H\ll D)$ from a 3-D low elevation one-cylinder model.	SBR rays only, fixed Tx, 2-D mobile Rx, 2-D MIMO, 3-D non-isotropic scattering (isotropic in the elevation domain).	$K=0$, $\eta_{\mathrm{SBT}}=0$, $\eta_{\mathrm{DB}}=0$, $v_T=0$, $\xi_R=0$, $\psi_T=\psi_R=0$, $k_T=k_R=0$, $\beta_{Tm}=0$.

are obtained under $M_T=M_R=1$, $p=p'=1$, $q=q'=1$, $f_c=250$ MHz, $f_{T\max}=f_{R\max}=80$ Hz, $\gamma_T=\gamma_R=90^{\circ}$, $\xi_T=\xi_R=0^{\circ}$, $\boldsymbol{d}_{TR}=[0, 2000\text{ m}, 1600\text{ m}-1600\text{ m}]^{\mathrm{T}}=[0, 2000\text{ m}, 0]^{\mathrm{T}}$, $R_1=R_2=8$ m, $k_T=k_R=5$, $\alpha_{T\mu}=90^{\circ}$, $\alpha_{R\mu}=270^{\circ}$, $\beta_{Tm}=\beta_{Rm}=15^{\circ}$, and $\beta_{T\mu}=\beta_{R\mu}=-30^{\circ}$, $K=6.5$, $\eta_{\mathrm{SBT}}=\eta_{\mathrm{SBR}}=0$, and $\eta_{\mathrm{DB}}=1$.

As can be seen from Fig. 3, the theoretical spectral curves match well the measured data points, which justifies the utility of our ST-CF. But it should be pointed out that, as analyzed and concluded in [47], this A2A measurement campaign was conducted at a rather high altitude; therefore, the major scattering objects that surround each station are the wings on the aircraft itself (which is why we set R_1 and R_2 to 8 m that is approximately half of the wingspan) and the propagating waves mainly consisted of a LoS path and a specular reflected path. As a result, it might be

TABLE III
SOME CORRELATION FUNCTIONS OBTAINED FROM THE TWO-RING AND THE TWO-CYLINDER MODEL THAT ARE SPECIAL CASES OF THE ST-CF DERIVED IN THIS ARTICLE

Ref.	Expression	Description	Condition
[40]	$J_0\left(2\pi f_{T\max}\tau\right) J_0\left(2\pi f_{R\max}\tau\right)$, from a 2-D two-ring model.	DB rays only, 2-D mobile Tx and Rx, SISO, 2-D isotropic scattering.	$K=0$, $\eta_{\text{SBT}}=0$, $\eta_{\text{SBR}}=0$, $\xi_T=\xi_R=0$, $d_T=d_R=0$, $k_T=k_R=0$, $\beta_{Tm}=\beta_{Rm}=0$.
[38]	$J_0\left(\frac{2\pi}{\lambda}d_T\right) J_0\left(\frac{2\pi}{\lambda}d_R\right)$, from a 2-D two-ring model.	DB rays only, fixed Tx and Rx, 2-D MIMO, 2-D isotropic scattering.	$K=0$, $\eta_{\text{SBT}}=0$, $\eta_{\text{SBR}}=0$, $v_T=v_R=0$, $\psi_T=\psi_R=0$, $k_T=k_R=0$, $\beta_{Tm}=\beta_{Rm}=0$.
[41]	$\frac{I_0\left(\sqrt{x^2+y^2}\right)}{I_0(k_T)}\frac{I_0\left(\sqrt{z^2+w^2}\right)}{I_0(k_R)}$, where $x=-j\frac{2\pi}{\lambda}\left(p-p'\right)d_T\cos\theta_T$ $-j2\pi f_{T\max}\tau\cos\gamma_T+k_T\cos\alpha_{T\mu}$, $y=-j\frac{2\pi}{\lambda}\left(p-p'\right)d_T\sin\theta_T$ $-j2\pi f_{T\max}\tau\sin\gamma_T+k_T\sin\alpha_{T\mu}$, $z=-j\frac{2\pi}{\lambda}\left(q-q'\right)d_R\cos\theta_R$ $-j2\pi f_{R\max}\tau\cos\gamma_R+k_R\cos\alpha_{R\mu}$, $w=-j\frac{2\pi}{\lambda}\left(q-q'\right)d_R\sin\theta_R$ $-j2\pi f_{R\max}\tau\sin\gamma_R+k_R\sin\alpha_{R\mu}$, from a 2-D two-ring model.	DB rays only, 2-D mobile Tx and Rx, 2-D MIMO, 2-D non-isotropic scattering.	$K=0$, $\eta_{\text{SBT}}=0$, $\eta_{\text{SBR}}=0$, $\xi_T=\xi_R=0$, $\psi_T=\psi_R=0$, $\beta_{Tm}=\beta_{Rm}=0$.
[29]	$\frac{I_0\left(\sqrt{x_1^2+y_1^2}\right)}{I_0(k_T)}\frac{\cos\left(\frac{2\pi}{\lambda}\beta_{Tm}d_{T_z}^{(p,p')}\right)}{1-\left(\frac{4\beta_{Tm}d_{T_z}^{(p,p')}}{\lambda}\right)^2}$ $\frac{I_0\left(\sqrt{z_1^2+w_1^2}\right)}{I_0(k_R)}\frac{\cos\left(\frac{2\pi}{\lambda}\beta_{Rm}d_{R_z}^{(q,q')}\right)}{1-\left(\frac{4\beta_{Rm}d_{R_z}^{(q,q')}}{\lambda}\right)^2}$, where $x_1=j2\frac{2\pi}{\lambda}d_{T_x}^{(p,p')}-j2\pi f_{T\max}\cos\gamma_T+k_T\cos\alpha_{T\mu}$, $y_1=j2\frac{2\pi}{\lambda}d_{T_y}^{(p,p')}-j2\pi f_{T\max}\sin\gamma_T+k_T\sin\alpha_{T\mu}$, $z_1=j2\frac{2\pi}{\lambda}d_{R_x}^{(q,q')}-j2\pi f_{R\max}\cos\gamma_R+k_R\cos\alpha_{R\mu}$, $w_1=j2\frac{2\pi}{\lambda}d_{R_y}^{(q,q')}-j2\pi f_{R\max}\sin\gamma_R+k_T\sin\alpha_{R\mu}$, from a 3-D low elevation two-cylinder model.	DB rays only, 2-D mobile Tx and Rx, 3-D MIMO, 3-D non-isotropic scattering (zero mean in the elevation domain).	$K=0$, $\eta_{\text{SBT}}=0$, $\eta_{\text{SBR}}=0$, $\xi_T=\xi_R=0$, $\beta_{T\mu}=\beta_{R\mu}=0$.
[42]	$\frac{K}{K+1}e^{j\frac{2\pi}{\lambda}\left(-\left(p-p'\right)d_T\cos\theta_T+\left(q-q'\right)d_R\cos\theta_R\right)}$ $\cdot e^{j2\pi\tau\left(-f_{T\max}\cos\gamma_T+f_{R\max}\cos\gamma_R\right)}$ $+\frac{\eta_{\text{SBT}}}{K+1}e^{j2\pi\left(\left(q-q'\right)\frac{d_R}{\lambda}\cos\theta_R+f_{R\max}\tau\cos\gamma_R\right)}\frac{I_0\left(\sqrt{x_{\text{SBT}}^2+y_{\text{SBT}}^2}\right)}{I_0(k_T)}$ $+\frac{\eta_{\text{SBR}}}{K+1}e^{-j2\pi\left(\left(p-p'\right)\frac{d_T}{\lambda}\cos\theta_T+f_{T\max}\tau\cos\gamma_T\right)}\frac{I_0\left(\sqrt{x_{\text{SBR}}^2+y_{\text{SBR}}^2}\right)}{I_0(k_T)}$ $+\frac{\eta_{\text{DB}}}{K+1}\frac{I_0\left(\sqrt{x_{\text{DB}}^2+y_{\text{DB}}^2}\right)}{I_0(k_T)}\frac{I_0\left(\sqrt{z_{\text{DB}}^2+w_{\text{DB}}^2}\right)}{I_0(k_R)}$, where $x_{\text{SBT}}=-j\frac{2\pi}{\lambda}\left(p-p'\right)d_T\cos\theta_T$ $-j2\pi f_{T\max}\tau\cos\gamma_T+k_T\cos\alpha_{T\mu}$, $y_{\text{SBT}}=-j\frac{2\pi}{\lambda}\left(\left(p-p'\right)d_T\sin\theta_T+\left(q-q'\right)d_R\Delta_T\sin\theta_R\right)$ $-j2\pi\tau\left(f_{T\max}\sin\gamma_T+f_{R\max}\Delta_T\sin\gamma_R\right)+k_T\sin\alpha_{T\mu}$, $x_{\text{SBR}}=-j\frac{2\pi}{\lambda}\left(q-q'\right)d_R\cos\theta_R$ $-j2\pi f_{R\max}\tau\cos\gamma_R+k_R\cos\alpha_{R\mu}$, $y_{\text{SBR}}=-j\frac{2\pi}{\lambda}\left(\left(p-p'\right)d_R\Delta_R\sin\theta_T+\left(q-q'\right)d_R\sin\theta_R\right)$ $-j2\pi\tau\left(f_{T\max}\Delta_R\sin\gamma_T+f_{R\max}\sin\gamma_R\right)+k_R\sin\alpha_{R\mu}$, where $x_{\text{DB}}=-j\frac{2\pi}{\lambda}\left(p-p'\right)d_T\cos\theta_T$ $-j2\pi f_{T\max}\tau\cos\gamma_T+k_T\cos\alpha_{T\mu}$, $y_{\text{DB}}=-j\frac{2\pi}{\lambda}\left(p-p'\right)d_T\sin\theta_T$ $-j2\pi f_{T\max}\tau\sin\gamma_T+k_T\sin\alpha_{T\mu}$, $z_{\text{DB}}=-j\frac{2\pi}{\lambda}\left(q-q'\right)d_R\cos\theta_R$ $-j2\pi f_{R\max}\tau\cos\gamma_R+k_R\cos\alpha_{R\mu}$, $w_{\text{DB}}=-j\frac{2\pi}{\lambda}\left(q-q'\right)d_R\sin\theta_R$ $-j2\pi f_{R\max}\tau\sin\gamma_R+k_R\sin\alpha_{R\mu}$, $(\Delta_T\approx R_1/D,\ \Delta_R\approx R_2/D)$ from a 2-D two-ring model.	LoS, SBT, SBR, DB rays, 2-D mobile Tx and Rx, 2-D MIMO, 2-D non-isotropic scattering.	$\xi_T=\xi_R=0$, $\psi_T=\psi_R=0$, $\beta_{Tm}=\beta_{Rm}=0$.

more appropriate to characterize this A2A channel using a two-path channel model. Unfortunately, the ground reflection was neglected in our geometrical model; accounting for this is also a future topic. Nevertheless, the good agreements presented in Fig. 3 indicate that the effect of the specular reflection can be converted to those of the scattered rays equivalently, provided that the values of the scattering-related parameters are properly chosen. And for this particular reason, the parameters $\alpha_{T\mu}$, $\alpha_{R\mu}$, β_{Tm}, β_{Rm}, $\beta_{T\mu}$, and $\beta_{R\mu}$ have been set to cover the rays reflected from the ground. The other parameters have also been carefully selected to represent the measured environment as faithfully as possible. For example, the values of the parameters f_c and $\boldsymbol{d}_{TR}$ γ_T, γ_R, ξ_T, and ξ_R are set according to the measurement description in [47], and the values of the parameters $f_{T\max}$ and $f_{R\max}$ are based on the specifications of the aircraft models used in [47].

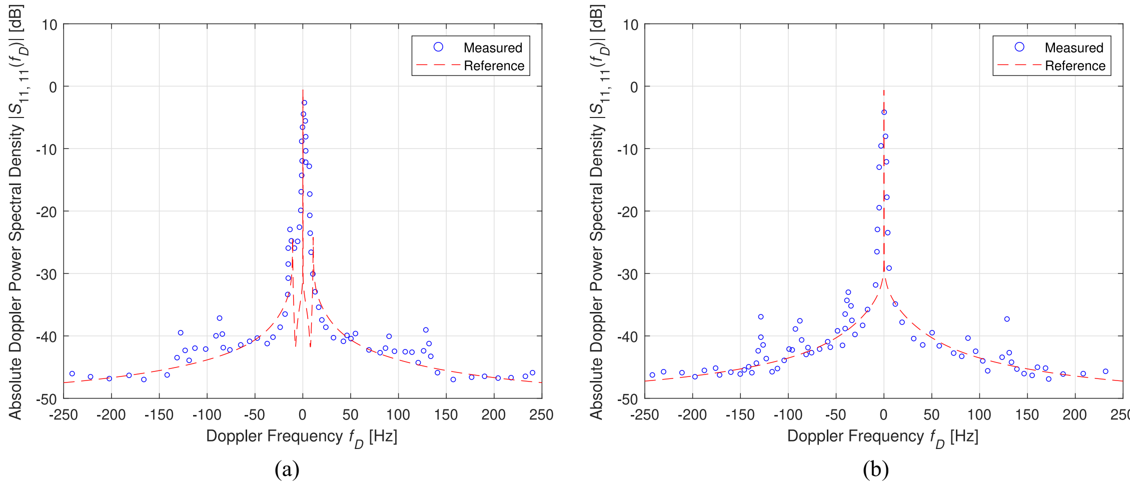

Fig. 3. Comparison between the theoretical Doppler PSDs and measurement data reported in [47] for (a) urban terrain and (b) grassland terrain. The additional peaks caused by reflections on the rotor blades cannot be captured by the proposed model.

While the small-size rotary-wing UAVs have been considered as a promising candidate for future communication networks, the related U2U channel measurement is still widely missing in literature. Because of the lack of reported measured data on such U2U channels, it is infeasible for us to perform a comparison to the proposed channel model at this time. Nevertheless, for future reference, we would like to provide some empirical rules here regarding the parameter setting of the proposed channel model for low-altitude small rotorcraft-enabled U2U communications in urban scenarios and rural scenarios. In urban areas, there are plenty of buildings and obstacles around the UAV stations. This indicates that the the value of the Ricean factor K is low, and that the DB rays bear more energy than the single-bounced rays, i.e., $\eta_{\mathrm{DB}} > \max\{\eta_{\mathrm{SBT}}, \eta_{\mathrm{SBR}}\}$. In addition, due to the dense scattering in the urban scenario, the values of the concentration parameters k_T and k_R in the scatterers' distribution are relatively small as the scattered waves shall come from many possible directions. On the contrary, the scattering in the rural scenario is usually sparse since the natural forests or mountains are not so orderly distributed as the man-made structures, which means that the values of the concentration parameters k_T and k_R are comparatively large. Besides, rural areas often have plenty of open space that is free of scattering, which implies that the value of the Ricean factor K is relatively high and that the single-bounced rays would bear more energy than the DB rays, i.e., $\max\{\eta_{\mathrm{SBT}}, \eta_{\mathrm{SBR}}\} > \eta_{\mathrm{DB}}$.

III. Simulation Models for U2U MIMO Channels

In this section, we consider a finite number of scatterers to develop practical yet accurate simulation models, i.e., channel simulators, where the complex channel gain becomes

$$\hat{h}_{pq}(t) = \sqrt{\frac{K}{K+1}}\hat{h}^{\mathrm{LoS}}_{pq}(t) + \sqrt{\frac{\eta_{\mathrm{SBT}}}{K+1}}\hat{h}^{\mathrm{SBT}}_{pq}(t) + \sqrt{\frac{\eta_{\mathrm{SBR}}}{K+1}}\hat{h}^{\mathrm{SBR}}_{pq}(t) + \sqrt{\frac{\eta_{\mathrm{DB}}}{K+1}}\hat{h}^{\mathrm{DB}}_{pq}(t) \quad (45)$$

where $\hat{h}^{\mathrm{LoS}}_{pq}(t)$, $\hat{h}^{\mathrm{SBT}}_{pq}(t)$, $\hat{h}^{\mathrm{SBR}}_{pq}(t)$, and $\hat{h}^{\mathrm{DB}}_{pq}(t)$ denote the simulated channel gains for the LoS, SBT, SBR, and DB rays, respectively.

Since the LoS rays have nothing to do with the scatterers, the expression of $\hat{h}^{\mathrm{LoS}}_{pq}(t)$ is the same as (6), i.e.,

$$\hat{h}^{\mathrm{LoS}}_{pq}(t) \approx e^{-j\frac{2\pi}{\lambda}\left(|\boldsymbol{d}_{TR}|+\hat{\boldsymbol{d}}_{TR}\cdot(-\boldsymbol{d}_{Tp}+\boldsymbol{d}_{Rq})\right)} e^{j2\pi\left(f_{T\max}\cos\langle\boldsymbol{v}_T,\boldsymbol{d}_{TR}\rangle - f_{R\max}\cos\langle\boldsymbol{v}_R,\boldsymbol{d}_{TR}\rangle\right)t}. \quad (46)$$

Simulating the SBT components can be done by removing the limit symbol in (7) and, thereby, the expression of $\hat{h}^{\mathrm{SBT}}_{pq}(t)$ can be written as

$$\hat{h}^{\mathrm{SBT}}_{pq}(t) \approx \frac{1}{\sqrt{N_1}}\sum_{n_1=1}^{N_1} e^{j\phi_{n_1}} e^{-j\frac{2\pi}{\lambda}\left(|\boldsymbol{d}_{Tn_1}|+|\boldsymbol{d}_{n_1R}|-\hat{\boldsymbol{d}}_{Tn_1}\cdot\boldsymbol{d}_{Tp}+\hat{\boldsymbol{d}}_{n_1R}\cdot\boldsymbol{d}_{Rq}\right)} e^{j2\pi\left(f_{T\max}\cos\langle\boldsymbol{v}_T,\boldsymbol{d}_{pn_1}\rangle - f_{R\max}\cos\langle\boldsymbol{v}_R,\boldsymbol{d}_{n_1q}\rangle\right)t}. \quad (47)$$

Similarly, the expression of $\hat{h}^{\mathrm{SBR}}_{pq}(t)$ is given by

$$\hat{h}^{\mathrm{SBR}}_{pq}(t) \approx \frac{1}{\sqrt{N_2}}\sum_{n_2=1}^{N_2} e^{j\phi_{n_2}} e^{-j\frac{2\pi}{\lambda}\left(|\boldsymbol{d}_{Tn_2}|+|\boldsymbol{d}_{n_2R}|-\hat{\boldsymbol{d}}_{Tn_2}\cdot\boldsymbol{d}_{Tp}+\hat{\boldsymbol{d}}_{n_2R}\cdot\boldsymbol{d}_{Rq}\right)} e^{j2\pi\left(f_{T\max}\cos\langle\boldsymbol{v}_T,\boldsymbol{d}_{Tn_2}\rangle - f_{R\max}\cos\langle\boldsymbol{v}_R,\boldsymbol{d}_{n_2R}\rangle\right)t}. \quad (48)$$

Finally, the expression of $\hat{h}^{\mathrm{DB}}_{pq}(t)$ is

$$\hat{h}^{\mathrm{DB}}_{pq}(t) \approx \frac{1}{\sqrt{N_1N_2}}\sum_{n_1=1}^{N_1}\sum_{n_2=1}^{N_2} e^{j\phi_{n_1n_2}} e^{-j\frac{2\pi}{\lambda}\left(|\boldsymbol{d}_{Tn_1}|+|\boldsymbol{d}_{n_1n_2}|+|\boldsymbol{d}_{n_2R}|-\hat{\boldsymbol{d}}_{Tn_1}\cdot\boldsymbol{d}_{Tp}+\hat{\boldsymbol{d}}_{n_2R}\cdot\boldsymbol{d}_{Rq}\right)} e^{j2\pi\left(f_{T\max}\cos\langle\boldsymbol{v}_T,\boldsymbol{d}_{Tn_1}\rangle - f_{R\max}\cos\langle\boldsymbol{v}_R,\boldsymbol{d}_{n_2R}\rangle\right)t}. \quad (49)$$

Note that the expressions of the vectors shown above contain the discrete AoDs and the discrete AoAs.

A. Deterministic Simulation Model

We design a deterministic simulation model by generating the AoDs and AoAs as

$$\alpha_T^{(n_{1,A})} = F_{\alpha_T}^{-1}\left(\frac{n_{1,A}-\frac{1}{2}}{N_{1,A}}\right) \tag{50}$$

$$\alpha_R^{(n_{2,A})} = F_{\alpha_R}^{-1}\left(\frac{n_{2,A}-\frac{1}{2}}{N_{2,A}}\right) \tag{51}$$

$$\beta_T^{(n_{1,E})} = \beta_{T\mu} + \frac{2\beta_{Tm}}{\pi}\arcsin\left(\frac{2\left(n_{1,E}-\frac{1}{2}\right)}{N_{1,E}}-1\right) \tag{52}$$

$$\beta_R^{(n_{2,E})} = \beta_{R\mu} + \frac{2\beta_{Rm}}{\pi}\arcsin\left(\frac{2\left(n_{2,E}-\frac{1}{2}\right)}{N_{2,E}}-1\right) \tag{53}$$

for $n_{1,A} = 1, 2, \ldots, N_{1,A}$, $n_{2,A} = 1, 2, \ldots, N_{2,A}$, $n_{1,E} = 1, 2, \ldots, N_{1,E}$, and $n_{2,E} = 1, 2, \ldots, N_{2,E}$, respectively, where $N_1 = N_{1,A}N_{1,E}$ and $N_2 = N_{2,A}N_{2,E}$. Note that $F_{\alpha_T}^{-1}(\cdot)$ and $F_{\alpha_R}^{-1}(\cdot)$ stand for the inverse functions of the von Mises cumulative distribution functions for $\alpha_T^{(n_1)}$ and $\alpha_R^{(n_2)}$, respectively. In this model, the simulated angles maintain unchanged for different simulation trials and, hence, only one trial is required to obtain the results. However, such simulators do not confirm to the reality that scatterers are not always fixed.

B. Stochastic Simulation Model

For better accordance with the reality, we propose a stochastic simulator by introducing randomness into the simulation:

$$\alpha_T^{(n_{1,A})} = F_{\alpha_T}^{-1}\left(\frac{n_{1,A}+\left(\theta_{1,A}-\frac{1}{2}\right)-\frac{1}{2}}{N_{1,A}}\right) \tag{54}$$

$$\alpha_R^{(n_{2,A})} = F_{\alpha_R}^{-1}\left(\frac{n_{2,A}+\left(\theta_{2,A}-\frac{1}{2}\right)-\frac{1}{2}}{N_{2,A}}\right) \tag{55}$$

$$\beta_T^{(n_{1,E})} = \beta_{T\mu} + \frac{2\beta_{Tm}}{\pi}\arcsin\left(\frac{2\left(n_{1,E}+\theta_{1,E}-1\right)}{N_{1,E}}-1\right) \tag{56}$$

$$\beta_R^{(n_{2,E})} = \beta_{R\mu} + \frac{2\beta_{Rm}}{\pi}\arcsin\left(\frac{2\left(n_{2,E}+\theta_{2,E}-1\right)}{N_{2,E}}-1\right) \tag{57}$$

for $n_{1,A} = 1, 2, \ldots, N_{1,A}$, $n_{2,A} = 1, 2, \ldots, N_{2,A}$, $n_{1,E} = 1, 2, \ldots, N_{1,E}$, and $n_{2,E} = 1, 2, \ldots, N_{2,E}$, respectively, where $N_1 = N_{1,A}N_{1,E}$ and $N_2 = N_{2,A}N_{2,E}$. Note that $\theta_{1,A}$, $\theta_{2,A}$, $\theta_{1,E}$, and $\theta_{2,E}$ are independent random variables uniformly distributed over $[0, 1)$. The results from this stochastic model vary for different trials, but averaging them over a sufficient number of trials will show us the ensemble properties.

IV. Capacity Analysis for U2U MIMO Channels

Suppose no channel state information (CSI) at the Tx and full CSI at the Rx, and the ergodic capacity is defined as

$$C_{\text{erg}} = \mathbb{E}\left[\log_2 \det\left(\mathbf{I}_{M_R} + \frac{\rho}{M_T}\mathbf{H}(t)\mathbf{H}^\dagger(t)\right)\right] \tag{58}$$

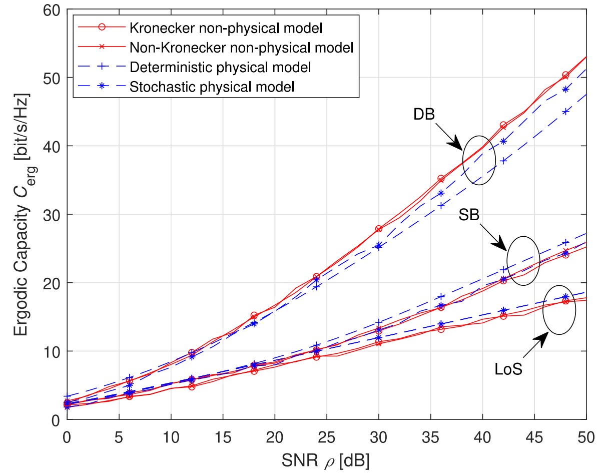

Fig. 4. Comparisons of ergodic capacities obtained from the Kronecker nonphysical model, the non-Kronecker nonphysical, the deterministic physical model, and the stochastic physical model for the LoS case, the SB case, and the DB case under $M_T = M_R = 4$. As expected, the DB rays provide larger capacity than the SB rays, and the SB rays larger than the LoS rays.

where it is assumed that $M_T \geq M_R$, $\mathbf{I}_{M_R}$ is the $M_R \times M_R$ identity matrix, ρ is the mean signal-to-noise ratio (SNR), and $\mathbf{H}(t) = [H_{ij}(t)]_{M_R \times M_T}$ is the $M_R \times M_T$ MIMO channel matrix. There are two main approaches to generate the matrix $\mathbf{H}$ for U2U MIMO channels. One is to use[2] $H_{ij}(t) = \hat{h}_{ji}(t)$ given by the channel simulators as in (45), and this simulator-based approach has two different methods: 1) the deterministic model and 2) the stochastic model, depending on the type of the simulator used to produce the entries of $\mathbf{H}$. The other approach is to exploit the correlation matrix easily obtainable from the closed-form ST-CFs that we have discussed in Section II, and this correlation-based approach also involves two commonly used methods: 1) the Kronecker model $\mathbf{H} = \mathbf{R}_R^{1/2}\mathbf{H}_\mathbf{w}\mathbf{R}_T^{\mathrm{T}/2}$ [49, eq. (4.77)] and 2) the more general non-Kronecker model $\text{vec}(\mathbf{H}) = \mathbf{R}^{1/2}\text{vec}(\mathbf{H}_\mathbf{w})$ [50, eq. (5.16)], where $\mathbf{H}_\mathbf{w}$ is an $M_R \times M_T$ white complex Gaussian matrix, $\mathbf{R}_R$ is the $M_R \times M_R$ receive correlation matrix, $\mathbf{R}_T$ is the $M_T \times M_T$ receive correlation matrix, and $\mathbf{R}_R$ is the $M_TM_R \times M_TM_R$ complete correlation matrix. The elements of these correlation matrices can be obtained using (11) [49, eqs. 4.71, 4.72, and 4.73], with (16) and (30)–(32) substituted and the argument τ set to 0 [28], [29]. These correlation-based models have lower complexity and higher generality than the simulator-based ones, but, on the other hand, preserves less information about the physical structure of the channels compared to the simulator-based ones [49, p. 190]. Hence, we will refer to the correlation-based models as (Kronecker or non-Kronecker) nonphysical models, whereas the simulator-based models as (deterministic or stochastic) physical models.

We are interested in whether the ergodic capacities resulted from these models agree with one another. Before going into that, it is noteworthy that the energy-related parameters K,

[2] In the subsequent substitution $H_{ij}(t) = \hat{h}_{ji}(t)$, the order of the two letters i and j in the subscripts of $\hat{h}_{ji}(t)$ is the opposite of that in the subscripts of H_{ij}. This is because in the commonly used definition of the channel matrix $\mathbf{H}$, the entries H_{ij} are complex channel gains from the jth transmit to the ith receive antenna [48, eq. (20.28)].

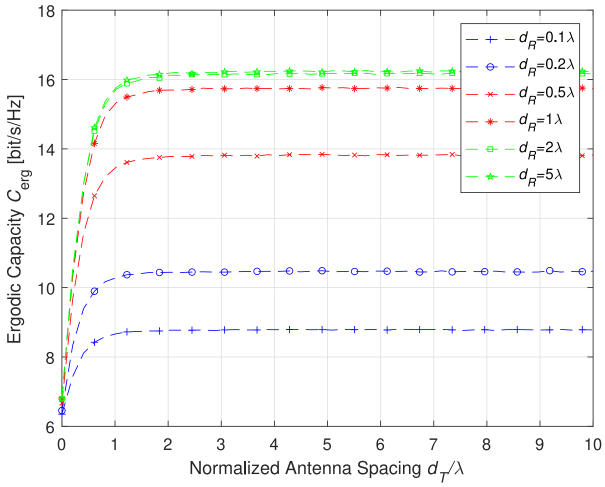

(a)

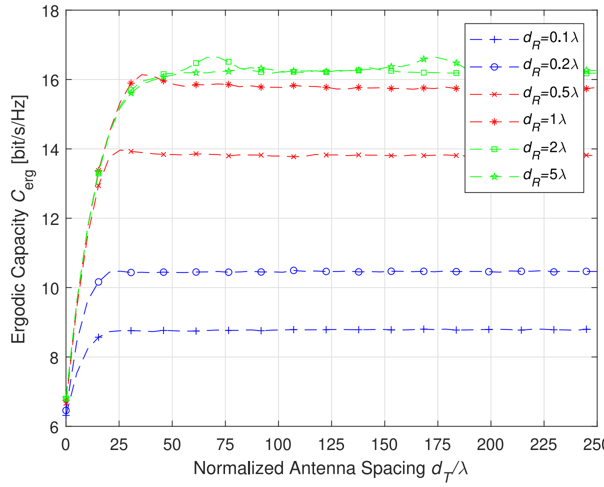

(b)

Fig. 5. Ergodic capacity versus the antenna spacings of the antenna arrays for (a) DB case and (b) SB case.

η_{SBT}, η_{SBR}, and η_{DB} have significant impacts on the total channel gains. However, it is not easy to give the typical values of these parameters as the work on U2U channel measurement is in its infancy. Under the circumstances, the best option for us is to start from the simplest cases: 1) pure LoS: $K = 1$, $\eta_{\mathrm{SBT}} = 0$, $\eta_{\mathrm{SBR}} = 0$, and $\eta_{\mathrm{DB}} = 0$; 2) pure SB(R):[3] $K = 0$, $\eta_{\mathrm{SBT}} = 0$, $\eta_{\mathrm{SBR}} = 1$, and $\eta_{\mathrm{DB}} = 0$; and 3) pure DB: $K = 0$, $\eta_{\mathrm{SBT}} = 0$, $\eta_{\mathrm{SBR}} = 0$, and $\eta_{\mathrm{DB}} = 1$. Since the channel gain in any other case is actually the linear combination of those in these basic cases, it is not difficult to extend to the general cases with arbitrary values of the energy-related parameters.

Fig. 4 shows the ergodic capacities obtained from the physical models and the nonphysical models for three basic cases: (pure) LoS, SB, and DB, where the parameters that we use are $M_T = M_R = 4$, $\boldsymbol{d}_{TR} = [0, 50\ \mathrm{m}, -50\ \mathrm{m}]^{\mathrm{T}}$, $R_1 = R_2 = 2$ m, $d_T = d_R = 0.5\lambda$, $\theta_T = \theta_R = 45°$, $\psi_T = \psi_R = 30°$, $k_T = k_R = 5$, $\alpha_{T\mu} = 90°$, $\alpha_{R\mu} = 270°$, $\beta_{T\mu} = \beta_{R\mu} = 10°$, and $\beta_{Tm} = \beta_{Rm} = 15°$. The results from the two nonphysical models are averaged over $N_{\mathrm{stat}} = 50$ simulation trials. As for the two physical models, the deterministic one employs $N_1 = 150$ scatterers at the Tx side and $N_2 = 150$ scatterers at the Rx side, where $N_{1,A} = N_{2,A} = 30$ and $N_{1,E} = N_{2,E} = 5$, whereas the stochastic one uses $N_1 = N_2 = 60$, where $N_{1,A} = N_{2,A} = 20$ and $N_{1,E} = N_{2,E} = 3$. The results from the stochastic physical model are also averaged under $N_{\mathrm{stat}} = 50$. As shown in Fig. 4, for each of the three cases, the ergodic capacities from the four different models generally agree with each other,[4] which validates the simulation models and the theoretical expressions. For efficiency, we will use the non-Kronecker nonphysical model to evaluate the capacity. From (31) and (32), we can easily notice that the channel correlations for both the SB case and the DB case rely on some key parameters, e.g., the antenna spacings between two adjacent elements d_T and d_R, the azimuth orientations of the antenna arrays θ_T and θ_R, and the elevation orientations of the antenna arrays ψ_T and ψ_R, and it can be inferred that these parameters will affect the channel capacities. Hence, we would like to explore and compare the effects of them on the ergodic capacities for the SB case and the DB case.

Fig. 5 presents the ergodic capacity versus the antenna spacings of the antenna arrays, where the parameters are $\rho = 15$ dB, $M_T = M_R = 4$, $\boldsymbol{d}_{TR} = [0, 50\ \mathrm{m}, -50\ \mathrm{m}]^{\mathrm{T}}$, $R_1 = R_2 = 2$ m, $\theta_T = \theta_R = 45°$, $\psi_T = \psi_R = 30°$, $k_T = k_R = 5$, $\alpha_{T\mu} = 90°$ (only applicable for the DB case), $\alpha_{R\mu} = 270°$, $\beta_{T\mu} = \beta_{R\mu} = 10°$, and $\beta_{Tm} = \beta_{Rm} = 15°$. It can be seen observed from Fig. 5 that the ergodic capacities, whether the SB case or the DB case, monotonically increase with the antenna spacing d_T or d_R within the range of 0.1λ to 2λ. Specifically, for the DB case shown in Fig. 5(a), the capacity stabilizes at about 16 bit/s/Hz if the transmit or receive antenna spacing reaches 2λ or over. For the SB case, Fig. 5(b) shows that the capacity no longer increases if the receive antenna spacing exceeds 2λ, which is the same as the DB case, and that the transmit antenna spacing has to go beyond 50λ to achieve a relative steadiness of the ergodic capacity. It is surprising to note that these two seemingly unconnected antenna spacing thresholds are related by the parameter $\tilde{\Delta}_R = R_2/\cos\beta_{R\mu}/|\boldsymbol{d}_{TR}|$ that approximately equals $1/25$ in that specific case. This suggests that in the SB cases the transmit antennas and the receive ones are not in co-equal status, as the scatterers are only distributed at one side.

Fig. 6 exhibits the ergodic capacity versus the azimuth orientations of the antenna arrays, where $\alpha_{T\mu} = 90°$ and $\alpha_{R\mu} = 270°$ for Fig. 6(a), and (b) and $\alpha_{T\mu} = 70°$ and $\alpha_{R\mu} = 180°$ for Fig. 6(c) and (d). The other parameters are the same as those in Fig. 5. It can be seen from Fig. 6 that the variations in capacities with the antenna array's azimuth orientations are related to the mean angles of the scatterers' distributions in the azimuth domain for both the DB cases and the SB

[3]Recall (30) and (31), and we can see that it is not necessary to study the pure SBT case and the pure SBR case separately, because these two cases are interchangeably equivalent.

[4]Strictly speaking, the correlation function as in (30) or (31) is not Kronecker separable, which is why in Fig. 4 the discrepancy between the Kronecker nonphysical model and the non-Kronecker one for the SB case is larger than that for the DB case.

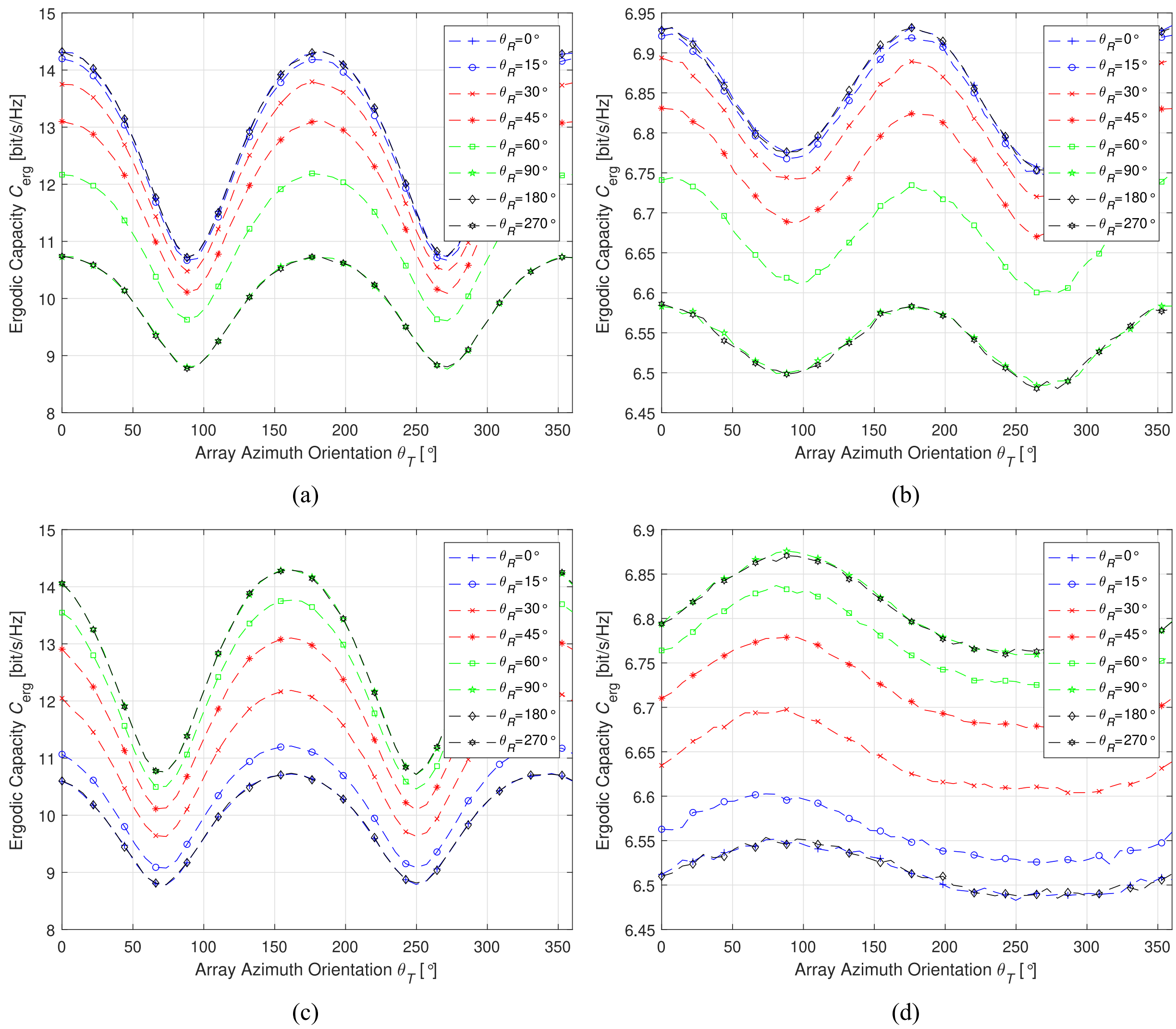

Fig. 6. Ergodic capacity versus the azimuth orientations of the antenna arrays for (a) DB case where $\alpha_{T\mu} = 90°$ and $\alpha_{R\mu} = 270°$, (b) SB case where $\alpha_{T\mu} = 90°$ and $\alpha_{R\mu} = 270°$, (c) DB case where $\alpha_{T\mu} = 70°$ and $\alpha_{R\mu} = 180°$, and (d) SB case where $\alpha_{T\mu} = 70°$ and $\alpha_{R\mu} = 180°$.

cases, and that there are noticeable differences in the variations between these two kinds of cases, though. By examining the peak values of the curves shown in Fig. 6(a) and (c), we know that for the DB cases, the maximum capacities with respect to θ_T arise when the condition $\theta_T - \alpha_{T\mu} = \pm 90°$; however, this rule appears not valid for the SB(R) cases as illustrated in Fig. 6(b) and (d) since the parameter $\alpha_{T\mu}$ plays no role in the SBR-only scattering environments. Besides, comparative inspections of the curves within Fig. 6 indicate that the maximum capacities with respect to θ_R emerge if $\theta_R - \alpha_{R\mu} = \pm 90°$, which is analogous to the DB situation regarding θ_T. Interestingly, different than the former one does, this θ_R-related rule applies to both the DB and the SB cases.

Fig. 7 displays the ergodic capacity versus the elevation orientations of the antenna arrays, where for Fig. 7(a) and (b), $k_T = k_R = 5$, and for Fig. 7(c) and (d), $k_T = k_R = 100$. The other parameters remain the same as those in Fig. 5. It is clear in Fig. 7 that the variations in capacities with the antenna array's elevation orientation are dependent of the dispersion level of the scatterers' distributions in the azimuth domain for both the DB cases and the SB ones, and that the dependence is quite different between the DB and the SB cases. For $k_T = k_R = 5$, the DB capacities reach the maximum when $\psi_T = 0°$ or $\psi_R = 0°$, while for $k_T = k_R = 100$, they reach the maximum when $\psi_T = 90°$ or $\psi_R = 90°$; however, although the SB capacities also reach the maximum when $\psi_T = 0°$ or $\psi_R = 0°$ for $k_T = k_R = 5$ and when $\psi_R = 0°$ for $k_T = k_R = 100$, they almost remain unchanged with ψ_T for $k_T = k_R = 100$. It can be inferred that, in weakly nonisotropic scattering environments, the antenna arrays should be placed horizontally; while in strongly nonisotropic scattering environments, the antenna arrays should be placed vertically.

V. Conclusion

In this article, we have proposed an arbitrary-elevation two-cylinder model for U2U MIMO channels. Based on this model, we have obtained a closed-form ST-CF that can be used to analyze the U2U channel capacity efficiently. We have shown that the SB rays and the DB ones have certain similarities but also significant differences in terms of how the capacities are

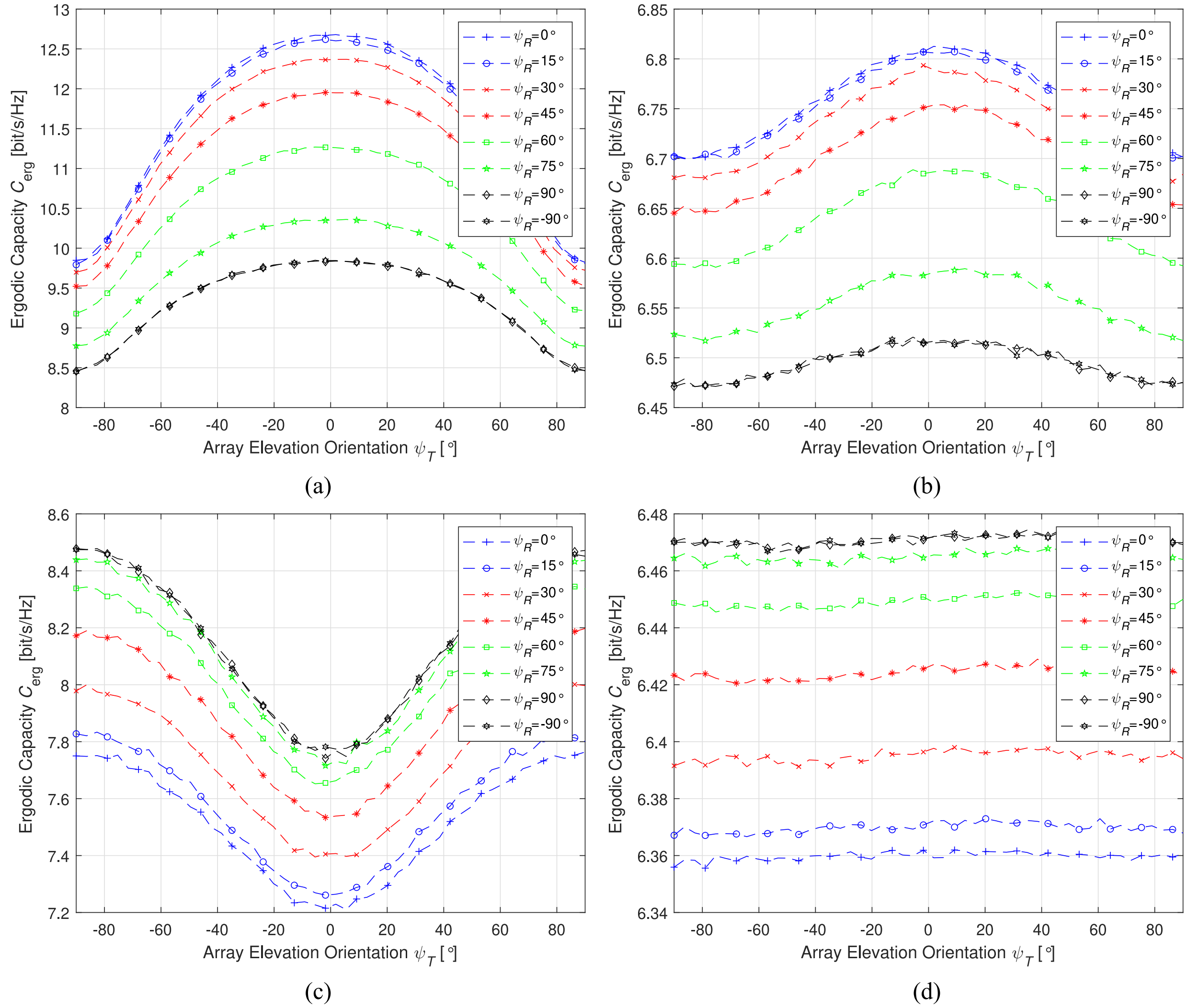

Fig. 7. Ergodic capacity versus the elevation orientations of the antenna arrays for (a) DB case where $k_T = k_R = 5$, (b) SB case where $k_T = k_R = 5$, (c) DB case where $k_T = k_R = 100$, and (d) SB case where $k_T = k_R = 100$.

affected by the model parameters. Hence, system setups should be altered according to the scattering environment (i.e., SB-dominant or DB-dominant) for better performance. Note that this work only discusses a narrowband channel model; to better facilitate the U2U system design, a future direction is to develop a wideband model where hopefully the channel characteristics can be derived into a closed form. In addition, since the UAV jitter/wobbling has shown a significant impact on high-frequency UAV channels, another interesting topic is to incorporate this effect in the proposed channel model.

References

[1] Y. Zeng, R. Zhang, and T. J. Lim, "Wireless communications with unmanned aerial vehicles: Opportunities and challenges," *IEEE Commun. Mag.*, vol. 54, no. 5, pp. 36–42, May 2016.

[2] J. Wang, C. Jiang, Z. Han, Y. Ren, R. G. Maunder, and L. Hanzo, "Taking drones to the next level: Cooperative distributed unmanned-aerial-vehicular networks for small and mini drones," *IEEE Veh. Technol. Mag.*, vol. 12, no. 3, pp. 73–82, Sep. 2017.

[3] J. Wang, C. Jiang, Z. Wei, C. Pan, H. Zhang, and Y. Ren, "Joint UAV hovering altitude and power control for space-air-ground IoT networks," *IEEE Internet Things J.*, vol. 6, no. 2, pp. 1741–1753, Apr. 2019.

[4] B. Li, Z. Fei, and Y. Zhang, "UAV communications for 5G and beyond: Recent advances and future trends," *IEEE Internet Things J.*, vol. 6, no. 2, pp. 2241–2263, Apr. 2019.

[5] G. Geraci et al., "What will the future of UAV cellular communications be? A flight from 5G to 6G," *IEEE Commun. Surveys Tuts.*, vol. 24, no. 3, pp. 1304–1335, 3rd Quart., 2022.

[6] C. Yan, L. Fu, J. Zhang, and J. Wang, "A comprehensive survey on UAV communication channel modeling," *IEEE Access*, vol. 7, pp. 107769–107792, 2019.

[7] J. Lyu and R. Zhang, "Network-connected UAV: 3-D system modeling and coverage performance analysis," *IEEE Internet Things J.*, vol. 6, no. 4, pp. 7048–7060, Aug. 2019.

[8] S. Lim, H. Yu, and H. Lee, "Optimal tethered-UAV deployment in A2G communication networks: Multi-agent Q-learning approach," *IEEE Internet Things J.*, vol. 9, no. 19, pp. 18539–18549, Oct. 2022.

[9] H. Jung, I.-H. Lee, and J. Joung, "Security energy efficiency analysis of analog collaborative beamforming with stochastic virtual antenna array of UAV swarm," *IEEE Trans. Veh. Technol.*, vol. 71, no. 8, pp. 8381–8397, Aug. 2022.

[10] M. M. Azari, G. Geraci, A. Garcia-Rodriguez, and S. Pollin, "UAV-to-UAV communications in cellular networks," *IEEE Trans. Wireless Commun.*, vol. 19, no. 9, pp. 6130–6144, Sep. 2020.

[11] H. Jiang, M. Mukherjee, J. Zhou, and J. Lloret, "Channel modeling and characteristics for 6G wireless communications," *IEEE Netw.*, vol. 35, no. 1, pp. 296–303, Jan./Feb. 2021.

[12] N. Goddemeier and C. Wietfeld, "Investigation of air-to-air channel characteristics and a UAV specific extension to the rice model," in *Proc. IEEE GLOBECOM Workshops*, San Diego, CA, USA, 2015, pp. 1–5.

[13] T. Liu et al., "Measurement-based characterization and modeling for low-altitude UAV air-to-air channels," *IEEE Access*, vol. 7, pp. 98832–98840, 2019.

[14] B. Ede et al., "Measurement-based large scale statistical modeling of air–to–air wireless UAV channels via novel time–frequency analysis," *IEEE Wireless Commun. Lett.*, vol. 11, no. 1, pp. 136–140, Jan. 2022.

[15] H. An et al., "Measurement and ray-tracing for UAV air-to-air channel modeling," in *Proc. IEEE ICEICT*, Hefei, China, 2022, pp. 415–420.

[16] N. E.-D. Safwat, I. M. Hafez, and F. Newagy, "Air-to-air channel model for UAVs in dense urban environments," in *Proc. ICEECCOT*, Mysuru, India, 2021, pp. 204–209.

[17] J. Supramongkonset, S. Duangsuwan, and S. Promwong, "A study of A2A channel modeling for small UAV-enabled wireless communication," in *Proc. ICEAST*, Chiang Mai, Thailand, 2022, pp. 01–04.

[18] Z. Ma, B. Ai, R. He, and Z. Zhong, "A 3D air-to-air wideband non-stationary channel model of UAV communications," in *Proc. IEEE VTC*, Honolulu, HI, USA, 2019, pp. 1–5.

[19] Z. Ma, B. Ai, R. He, G. Wang, Y. Niu, and Z. Zhong, "A wideband non-stationary air-to-air channel model for UAV communications," *IEEE Trans. Veh. Technol.*, vol. 69, no. 2, pp. 1214–1226, Feb. 2020.

[20] B. Yang and W. Zhang, "Analysis of propagation characteristics for MIMO air-to-air communications with UAV Jitter," in *Proc. ISAPE*, Zhuhai, China, 2021, pp. 1–4.

[21] Z. Ma et al., "Three-dimensional modeling of millimeter-wave MIMO channels for UAV-based communications," in *Proc. IEEE GLOBECOM*, Taipei, Taiwan, 2020, pp. 1–6.

[22] Z. Ma, B. Ai, R. He, Z. Zhong, and M. Yang, "A non-stationary geometry-based MIMO channel model for millimeter-wave UAV networks," *IEEE J. Sel. Areas Commun.*, vol. 39, no. 10, pp. 2960–2974, Oct. 2021.

[23] X. Zhang, J. Liu, F. Gu, D. Ma, and J. Wei, "An extended 3-D ellipsoid model for characterization of UAV air-to-air channel," in *Proc. IEEE ICC*, Shanghai, China, 2019, pp. 1–6.

[24] X. Mao, C.-X. Wang, and H. Chang, "A 3D non-stationary geometry-based stochastic model for 6G UAV air-to-air channels," in *Proc. WCSP*, Changsha, China, 2021, pp. 1–5.

[25] Y. Zhang, Y. Zhou, Z. Ji, K. Lin, and Z. He, "A three-dimensional geometry-based stochastic model for air-to-air UAV channels," in *Proc. VTC*, Victoria, BC, Canada, 2020, pp. 1–5.

[26] D.-S. Shiu, G. J. Foschini, M. J. Gans, and J. M. Kahn, "Fading correlation and its effect on the capacity of multielement antenna systems," *IEEE Trans. Commun.*, vol. 48, no. 3, pp. 502–513, Mar. 2000.

[27] A. Abdi and M. Kaveh, "A space-time correlation model for multielement antenna systems in mobile fading channels," *IEEE J. Sel. Areas Commun.*, vol. 20, no. 3, pp. 550–560, Apr. 2002.

[28] G. J. Byers and F. Takawira, "Spatially and temporally correlated MIMO channels: Modeling and capacity analysis," *IEEE Trans. Veh. Technol.*, vol. 53, no. 3, pp. 634–643, May 2004.

[29] A. G. Zajić and G. L. Stüber, "Three-dimensional modeling, simulation, and capacity analysis of space–time correlated mobile-to-mobile channels," *IEEE Trans. Veh. Technol.*, vol. 57, no. 4, pp. 2042–2054, Jul. 2008.

[30] L. Zeng, X. Cheng, C.-X. Wang, and X. Yin, "A 3D geometry-based stochastic channel model for UAV-MIMO channels," in *Proc. IEEE WCNC*, San Francisco, CA, USA, 2017, pp. 1–5.

[31] C. Ge, R. Zhang, D. Zhai, Y. Jiang, and B. Li, "UAV-correlated MIMO channels: 3-D geometrical-based polarized model and capacity analysis," *IEEE Internet Things J.*, vol. 10, no. 2, pp. 1446–1460, Jan. 2023.

[32] X. Cheng, C.-X. Wang, D. I. Laurenson, S. Salous, and A. V. Vasilakos, "An adaptive geometry-based stochastic model for non-isotropic MIMO mobile-to-mobile channels," *IEEE Trans. Wireless Commun.*, vol. 8, no. 9, pp. 4824–4835, Sep. 2009.

[33] Y. Yuan, C.-X. Wang, X. Cheng, B. Ai, and D. I. Laurenson, "Novel 3D geometry-based stochastic models for non-isotropic MIMO vehicle-to-vehicle channels," *IEEE Trans. Wireless Commun.*, vol. 13, no. 1, pp. 298–309, Jan. 2014.

[34] X. Cheng and Y. Li, "A 3-D geometry-based stochastic model for UAV-MIMO wideband nonstationary channels," *IEEE Internet Things J.*, vol. 6, no. 2, pp. 1654–1662, Apr. 2019.

[35] H. Jiang et al., "A novel 3D UAV channel model for A2G communication environments using AoD and AoA estimation algorithms," *IEEE Trans. Commun.*, vol. 68, no. 11, pp. 7232–7246, Nov. 2020.

[36] A. G. Zajić, G. L. Stüber, T. G. Pratt, and S. T. Nguyen, "Wideband MIMO mobile-to-mobile channels: Geometry-based statistical modeling with experimental verification," *IEEE Trans. Veh. Technol.*, vol. 58, no. 2, pp. 517–534, Feb. 2009.

[37] R. H. Clarke, "A statistical theory of mobile-radio reception," *Bell Syst. Tech. J.*, vol. 47, no. 6, pp. 957–1000, Jul./Aug. 1968.

[38] H. Kang, G. L. Stüber, T. G. Pratt, and M. A. Ingram, "Studies on the capacity of MIMO systems in mobile-to-mobile environment," in *Proc. IEEE WCNC*, Atlanta, GA, USA, 2004, pp. 363–368.

[39] S.-Y. Leong, Y. R. Zheng, and C. Xiao, "Space-time fading correlation functions of a 3-D MIMO channel model," in *Proc. IEEE WCNC*, Atlanta, GA, USA, 2004, pp. 1127–1132.

[40] A. S. Akki and F. Haber, "A statistical model of mobile-to-mobile land communication channel," *IEEE Trans. Veh. Technol.*, vol. 35, no. 1, pp. 2–7, Feb. 1986.

[41] A. G. Zajić and G. L. Stüber, "Space-time correlated MIMO mobile-to-mobile channels," in *Proc. IEEE ISPIMRC*, Helsinki, Finland, 2006, pp. 1–5.

[42] A. G. Zajić and G. L. Stüber, "Space-time correlated mobile-to-mobile channels: Modelling and simulation," *IEEE Trans. Veh. Technol.*, vol. 57, no. 2, pp. 715–726, Mar. 2008.

[43] I. S. Gradshteyn and I. M. Ryzhik, *Table of Integrals, Series, and Products*, 7th ed. Waltham, MA, USA: Academic, 2007.

[44] Z. Wei and J. Geng, "Time-variant PDFs of AODs and AOAs for ground scattering in low-altitude air-to-air communication over open area," *IEEE Commun. Lett.*, vol. 25, no. 3, pp. 701–705, Mar. 2021.

[45] B. Xiong, Z. Zhang, H. Jiang, J. Zhang, L. Wu, and J. Dang, "A 3D non-stationary MIMO channel model for reconfigurable intelligent surface auxiliary UAV-to-ground mmWave communications," *IEEE Trans. Wireless Commun.*, vol. 21, no. 7, pp. 5658–5672, Jul. 2022.

[46] H. Jiang, B. Xiong, H. Zhang, and E. Basar, "Physics-based 3D end-to-end modeling for double-RISs assisted non-stationary UAV-to-ground communication channels," *IEEE Trans. Commun.*, vol. 71, no. 7, pp. 4247–4261, Jul. 2023.

[47] M. Walter, S. Gligorević, T. Detert, and M. Schnell, "UHF/VHF air-to-air propagation measurements," in *Proc. EuCAP*, Barcelona, Spain, 2010, pp. 1–5.

[48] A. F. Molisch, *Wireless Communications*, 2nd ed. Chichester, U.K.: Wiley, 2012.

[49] T. Brown, P. Kyritsi, and E. De Carvalho, *Practical Guide to MIMO Radio Channel: With MATLAB Examples*. Chicester, U.K.: Wiley, 2012.

[50] J. R. Hampton, *Introduction to MIMO Communications*. Cambridge, U.K.: Cambridge Univ. Press, 2013.